Rotation and interaction of the CMEs of September 8 and 10, 2014, tested with EUHFORIA

Anwesha Maharana, Camilla Scolini, Brigitte Schmieder, Stefaan Poedts

**Astronomy &
Astrophysics**

Rotation and interaction of the CMEs of September 8 and 10, 2014, tested with EUHFORIA[*]

Anwesha Maharana[1,2] , Camilla Scolini[3] , Brigitte Schmieder[1,4], and Stefaan Poedts[1,5]

[1] Centre for mathematical Plasma Astrophysics (CmPA)/Dept. of Mathematics, KU Leuven, 3001 Leuven, Belgium
   e-mail: anwesha.maharana@kuleuven.be
[2] Royal Observatory of Belgium, 1180 Uccle, Belgium
[3] Institute for the Study of Earth, Oceans and Space, University of New Hampshire, 03824 Durham, NH, USA
[4] LESIA, Observatoire de Paris, Université PSL , CNRS, Sorbonne Université, Université Paris-Diderot, 92190 Meudon, France
[5] Institute of Physics, University of Maria Curie-Skłodowska, 20-031 Lublin, Poland

ABSTRACT

Context. Solar coronal mass ejections (CMEs) can catch up and interact with preceding CMEs and solar wind structures to undergo rotation and deflection during their propagation.
Aim. We aim to show how the interactions of a CME in the corona and heliosphere can play a significant role in altering its geoeffectiveness as predicted at the time of its eruption. To do so, we consider a case study of two successive CMEs launched from the active region NOAA 12158 in early September 2014. The second CME was predicted to be extensively geoeffective based on the remote-sensing observations of the source region. However, in situ measurements at 1 au recorded only a short-lasting, weak negative B_z component followed by a prolonged positive B_z component.
Methods. We used the EUropean Heliosphere FORecasting Information Asset (EUHFORIA) to perform a self-consistent 3D magnetohydrodynamical (MHD) data-driven simulation of the two CMEs in the heliosphere. First, the ambient solar wind is modelled, followed by the time-dependent injection of CME1 with the LFF spheromak and CME2 with the Flux Rope in 3D (FRi3D) model. The initial conditions of the CMEs are determined by combining observational insights near the Sun, which are fine-tuned to match the in situ observations near 1 au, with additional numerical experiments related to each individual CME.
Results. By introducing CME1 before CME2 in the EUHFORIA simulation, we modelled the negative B_z component in the sheath region ahead of CME2 whose formation can be attributed to the interaction between CME1 and CME2. To reproduce the positive B_z component in the magnetic ejecta of CME2, we had to initialise CME2 with an orientation determined at 0.1 au and consistent with the orientation interpreted at 1 au instead of the orientation observed during its eruption.
Conclusions. EUHFORIA simulations suggest the possibility of a significant rotation of CME2 in the low corona in order to explain the in situ observations at 1 au. Coherent magnetic field rotations with enhanced strength (potentially geoeffective) can be formed in the sheath region as a result of interactions between two CMEs in the heliosphere even if the individual CMEs are not geoeffective.

Key words. Sun: coronal mass ejections (CMEs) – Sun: heliosphere – Sun: magnetic fields – solar wind – solar-terrestrial relations – magnetohydrodynamics (MHD)

1. Introduction

Coronal mass ejections (CMEs) can drive major geomagnetic storms (Gosling et al. 1991; Huttunen et al. 2005). It is therefore important to model their initiation and propagation in order to forecast their arrival at Earth or at any other planet or satellite. Uncertainties in space weather prediction are introduced by multiple factors, beginning with the monitoring of the eruptions at the Sun, and subsequently the modelling of their propagation from the solar corona to the planets or satellites in the inner heliosphere (Riley & Ben-Nun 2021; Verbeke et al. 2022). Magnetohydrodynamic (MHD) modelling is useful for tracking the propagation of CMEs, and can be used to account for their interactions with solar wind structures and other CMEs and to compute their geoeffectiveness. Data-driven MHD modelling of CME evolution is more physical as it constrains the initial and boundary conditions using the early observations of the eruptions. However, if the orientation of the emerging CME is misinterpreted in the low corona, the initial conditions for the

propagation models will yield inappropriate prediction results. In this work, we present and analyse such a case of erroneous prediction of space weather, or 'space weather misprediction'. As part of the ISEST VarSITI campaign[1], the CME event of September 10, 2014, was used to perform the exercise of real-time forecasting. The prediction was made considering the magnetic field signatures of the eruption on the solar surface and the direction of propagation estimated from the coronagraphic field of view. The CME was predicted to have a strong negative B_z component and a frontal impact at Earth (Webb & Nitta 2017). However, by the time the CME reached Earth, the associated magnetic ejecta (ME; Burlaga 1988; Winslow et al. 2015) was characterised by a long-lasting positive B_z component. A brief period of negative B_z component was present in the sheath ahead of CME2, which drove a moderate storm (minimum Dst∼ −88 nT) instead of the predicted intense storm, and therefore predictions of the geoeffectiveness of the different substructures associated with the CME were largely inaccurate. Upon taking a

---

[*] Movie is available at https://www.aanda.org

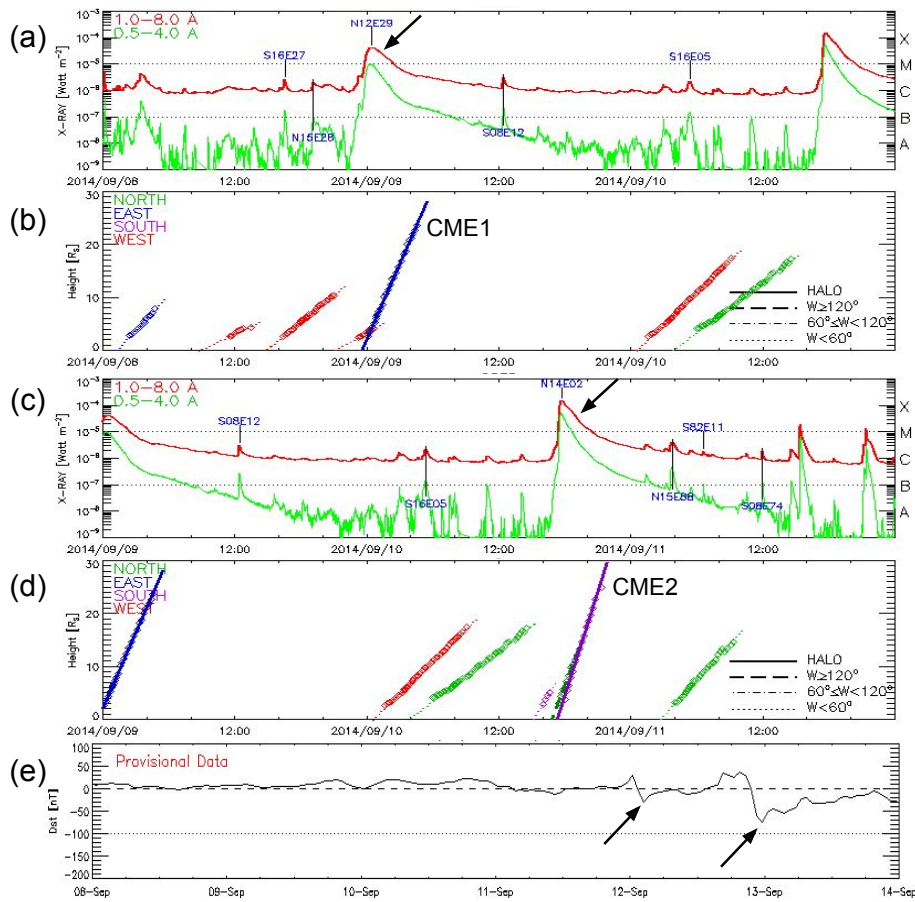[1] http://solar.gmu.edu/heliophysics/index.php/ISEST

Fig. 1. Overview of the eruption, early evolution in corona, and geomagnetic signatures of CME1 and CME2. Panels (a,b) and panels (c,d) span the time ranges of September 8–10, 2014, and September 9–11, 2014, respectively. (a) M-class flare on late September 8, 2014 (indicated with black arrow), which can be associated with the eruption of CME1. (b) Height-time plot of CME1 shown by the blue height profile starting at ~23.30 UT on September 8, 2014. (c) X-class flare on September 10 (indicated with black arrow), which can be associated with the eruption of CME2. (d) Height-time plot of CME2 shown by the purple height profile starting at ~17.30 UT on September 9, 2014. The solar source coordinates of the flares are labelled in the GOES X-ray intensity plots in panels (a,c). The colour (line) codes in panels (b,d) define the CME propagation direction (apparent angular width). (e) Disturbance storm index (Dst), a measure of the geomagnetic activity at Earth shows a calm phase followed by a mild disturbance and then a moderate storm in the period 12-14 September, 2014 (disturbances indicated with arrows). Source: CDAW catalogue – https://cdaw.gsfc.nasa.gov/CME_list/daily_plots/sephtx/2014_09/

closer look at this period, we noticed the presence of a preceding earthward CME that erupted late on September 8, 2014, and that was not recorded in any of the interplanetary CME (ICME) catalogues at Earth. It may be that this preceding CME preconditioned the propagation of the CME that erupted on September 10, 2014, suggesting that the CME–CME interaction may have led to the formation of the geoeffective sheath. Specifically, we are seeking answers to two questions: Firstly, we would like to determine the orientation of the CME that erupted on September 10, 2014, at 0.1 au that must be injected into the magnetohydrodynamic (MHD) heliospheric models like EUHFORIA (Pomoell & Poedts 2018) in order to obtain the correct magnetic field signatures at 1 au. Secondly, we seek to understand the role of the preceding CME in the formation of the negative B_z component (or the magnetic field rotation) in the sheath region.

The paper is organised as follows: In Sect. 2, we provide an observational overview of the event and present our motivation to carry out this study. In Sects. 3 and 4, we describe the event using various observational proxies, both remote and in situ, at the Sun ($1\,R_\odot$), close to 0.1 au, and at 1 au. We perform MHD simulations of the event as described in Sect. 5. Section 6 presents the modelling results and our interpretation of this

puzzling event, and in Sect. 7, we provide a summary of our findings and our conclusions.

2. Observations

2.1. Overview of Sun-to-Earth signatures of the CMEs

In this section, we identify the observational signatures of the two successive CMEs that occurred between September 8 and 10, 2014. The first CME (hereafter, CME1) was associated with an M4.6 flare occurring in the Active Region NOAA 12158 (hereafter, AR 12158), positioned at N12E29, on September 8, 2014, starting around 23:12 UT. The flare peaked at 00:28 UT on September 9, 2014. The origin of the second CME (hereafter, CME2) has been extensively studied (Cheng et al. 2015; Dudík et al. 2016; Zhao et al. 2016). CME2 was associated with an X1.6 flare that started on September 10, 2014, at 17:21 UT from AR 12158, positioned at N15E02, and peaked at 17:45 UT. Figures 1a and c indicate the flares and provide the X-ray intensities associated with the eruption of CME1 and CME2, respectively. The early propagation of both CME1 and CME2 was detected in the field of view (FOV) of the C2 and C3 instruments
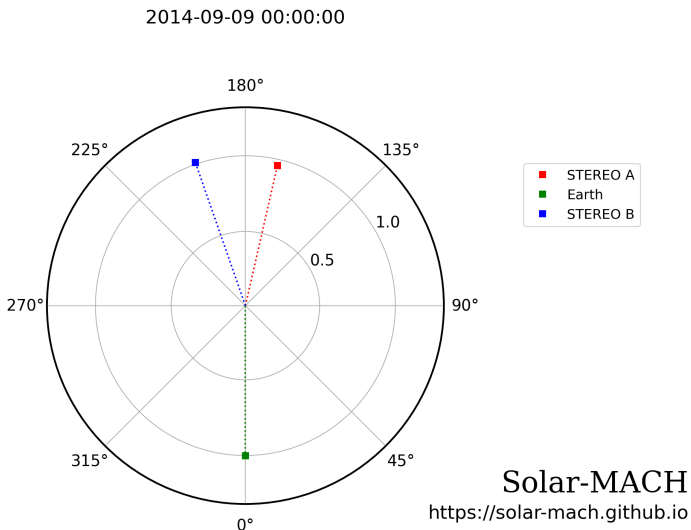
2014-09-09 00:00:00

Fig. 2. Position of STEREO-A, STEREO-B, and Earth on September 9, 2014, at 00:00. The grid in black corresponds to the Stonyhurst coordinate systems. This polar plot is generated using the Solar-MACH tool (https://serpentine-h2020.eu/tools/; Gieseler et al. 2022).

of the Large Angle and Spectrometric COronagraph (LASCO, Brueckner et al. 1995) on board the Solar and Heliospheric Observatory (SOHO), and the COR-2 instrument on board the Sun-Earth Connection Coronal and Heliospheric Investigation (SECCHI) package of the twin-spacecraft Solar Terrestrial Relations Observatory (STEREO, Kaiser et al. 2008). Only STEREO-B recorded the observations, while a data gap was found in STEREO-A during this period. Figure 2 shows the relative positioning of the observing spacecraft in the heliosphere. CME1 was visible in the C2 FOV at 00:06 UT with an apparent speed of 920 km s^{-1} and in COR-2B FOV at 00:24 UT. CME2 was first observed by C2 at 17:48 UT, and developed as a halo CME at 18:24 UT. It was later visible in the C3 FOV starting from around 18:45 UT with an apparent speed of 1267 km s^{-1}. CME2 also appeared for the first time in the FOV of COR-2B at 18:24 UT. The height-time profiles of CME1 and CME2 up to ∼30 $R_\odot$ created by automatic tracking of the CME leading edge, and fitted with an approximate linear profile by the CDAW catalogue are shown in Figs. 1b and d, respectively. The above details are also listed in Table 1. The association of the CMEs with the corresponding flares is also reported by Vemareddy et al. (2016a). Figure 3 shows the evolution of both CMEs in the C2 FOV. CME2, tagged as a 'textbook' event (Webb & Nitta 2017), reached Earth on September 12, 2014. The arrival of CME2 at L1 is recorded in the WIND ICME catalogue[2] at 15:17 UT and in the Richardson and Cane catalogue[3] (Cane & Richardson 2003; Richardson & Cane 2010) at 15:53 UT, respectively. The interplanetary counterpart of CME1 is not listed in any of the ICME catalogues. No other wide and Earthward CMEs were observed between the time period starting from the eruption of CME1 and two days after the eruption of CME2, which could have arrived at L1, interrupting or affecting the propagation of the two CMEs described here. Extrapolating the CME arrival times at Earth using the projected speeds from the CDAW catalogue[4], we obtain an interval time

between their estimated arrival times of about 29 h. This is a rough estimate assuming no effects from the drag and the interaction of the CMEs in the heliosphere affect their kinematics during propagation. The time difference between the arrival times observed in situ at L1 is ∼32 h, which corroborates the calculated time difference and the association between the coronal and interplanetary signatures of the eruptions. Signatures of both the CMEs were identified in the disturbance storm index (Dst) at Earth as shown in Fig. 1e. A low drop in Dst (∼−40 nT) followed by a moderately negative storm (Dst ∼−88 nT) was observed. This prompted the preliminary association of the CMEs in the low corona and the CMEs at 1 au.

2.2. In situ signatures at Earth

The in situ signatures of the CMEs are plotted in Fig. 4. The shock (S1) driven by CME1 is observed on September 11 at 22:50 UT based on the IPShock catalogue[5] (Kilpua et al. 2015) and is characterised by an enhancement in speed and number density. CME1 is directed north of the ecliptic plane as seen from the coronagraph images from the LASCO instruments[6]. The Space Weather Database Of Notifications, Knowledge, Information (DONKI)[7] catalogue has also recorded a northeastward launch direction of the CME. These observations suggest that the WIND spacecraft would have encountered the southwestern flank of CME1. The long sheath region (characterised by density enhancement and fluctuating magnetic field signatures in the red-shaded region in Fig. 4) after the shock of CME1 can also be inferred as the signature of the CME1 flank. Following these clear sheath signatures, we observe a simultaneous decrease in density and temperature, with plasma beta (β) being less than 1, and a slight apparent increase in the magnetic field after the turbulent phase. However, the lack of a clear rotation in the magnetic field vector suggests the passage of the CME1 flank. A period of bidirectional electrons can also be observed between S1 and S2 (corresponding to the yellow-shaded region), suggesting their propagation inside the magnetic ejecta (hereafter, ME1) associated with CME1. Although some other typical characteristics of MEs, such as a significantly enhanced magnetic field, clear rotations in the magnetic field components, and oxygen enhancements, are missing, the low density, temperature, and β, as well as the magnetic field fluctuations in combination with bidirectional electrons, suggest the passage of ME1 associated with CME1 starting on September 12 at 8:45 UT as indicated in the yellow shaded region (Zurbuchen & Richardson 2006). The second shock (S2) is recorded on September 12 at 15:17 UT. S2 is followed by a distinct turbulent sheath (green shaded region) and a clear magnetic ejecta (hereafter, ME2, shaded blue region). The start and end times of ME2, as recorded in the WIND catalogue, are September 12 at 21:22 UT and September 14 at 11:38 UT, respectively. The Richardson and Cane catalogue reports the ME2 boundaries as September 12 at 22:00 UT and September 14 at 2:00 UT. Upon closer visual inspection of the data, we find that the ME2 boundaries from the WIND catalogue include some part of the sheath before ME2, and the boundaries listed in the Richardson and Cane catalogue detect the end

---

Table 1. Observational details of the eruption of CME1 and CME2.

	CME1	CME2
Active region position	N12E29	N15E02
Flare class	M4.6	X1.6
Flare time (start - peak - end)	September 8, 23:12 UT – September 9, 00:28 UT – September 9, 01:30 UT	September 10, 17:21 UT – September 10, 17:45 UT – September 10, 17:45 UT
Apparent CME Speed [km s^{-1}]	920	1267

Notes. Flare details are as reported on Solar Monitor (`https://www.solarmonitor.org/`). The position of the active region AR 12158 according to the NOAA catalogue is in heliographic coordinates. CME speeds are taken from the CDAW catalogue as computed by an automatic linear fit.

of ME2 ~10 h earlier than the WIND catalogue. Although the WIND catalogue visibly provides better boundaries for ME2, we correct the start time to September 12 at 21:36 UT based on a visual inspection carried out in order to remove parts of the sheath. As seen in Fig. 4 (panel 1), a decreasing speed profile within ME2 points to an expanding structure passing through the spacecraft. Inside ME2, the plasma density and temperature are also reduced (Fig. 4, panel 2). Rotations in the magnetic field direction, an enhancement in the magnetic field strength, and a reduced β can also be observed in the shaded blue region in Fig. 4 (panels 3 and 4). The θ-profile (Fig. 4, panel 5) does not show a smooth rotation in the north-south magnetic field direction (i.e. $|\Delta\theta| \neq 0$), but rather a constant and long-duration positive profile. This observation is compatible with the passage of a CME flank. There is a jump in ϕ from 90° to >180° (Fig. 4, panel 6) which implies a westward axis of CME2. Marubashi et al. (2017) performed a toroidal CME model fitting to the in situ measurements of ME2 and reported a small rotation angle of the observed magnetic field vector. Their most important takeaway was that, although the magnetic field orientation of the CME2 is southward, the observed northward magnetic field inside ME2 could be due to the impact of the southern edge of the CME as the CME propagation was mainly north of the ecliptic. This highlights how crucial it is to predict what part of the gigantic CME would impact Earth in order to forecast the geomagnetic effects. A period of bidirectional suprathermal electrons corresponding to the ME2 boundaries can be observed (Fig. 4, panel 8). Other magnetic ejecta signatures, such as an enhanced oxygen charge ratio (O^{+7}/O^{+6}) and average iron charge ratio $\langle Q_F \rangle$ have also been reported in association with ME2 in Kilpua et al. (2021). The geomagnetic storms at L1 during the period of September 12–14, 2014, are characterised by the negative Dst index (Fig. 4, panel 7). The negative B_z component in the sheaths ahead of CME1 and CME2 can be associated with the weak storm on September 12 and the moderate storm on September 13, respectively.

Kilpua et al. (2021) modelled CME2 with a time-dependent magnetofrictional model initialised with a flux rope about the PIL as suggested by Vemareddy et al. (2016a) and with a chirality consistent with the inverse S-shaped extreme-ultraviolet (EUV) sigmoid. The modelling results did not match the in situ magnetic field observations. Although they inferred that CME2 was a flank hit at Earth, the extrapolated B_z component was still mainly negative contrary to the in situ observations at Earth. Some studies have shown that initialising CME2 in MHD heliospheric propagation models using the PIL orientation, as in Vemareddy et al. (2016a), did not match the magnetic field configuration at 1 au (An et al. 2019). The results from the previous studies raise the question of whether the CME rotated further anticlockwise –either in the low corona or during heliospheric
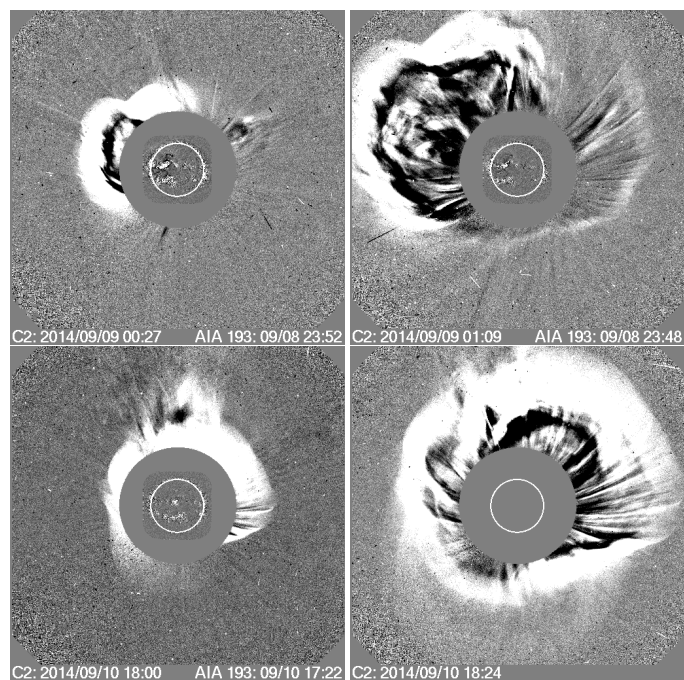

Fig. 3. Running difference images showing the development of CME1 (top row) on early September 9, 2014, and CME2 (bottom row) on September 10, 2014, in the LASCO C2 field of view. Source: `https://cdaw.gsfc.nasa.gov/CME_list/`

propagation– in a way that could have led to the passage of a westward axial magnetic field with a dominant positive B_z component through Earth.

3. Reconstruction of the CMEs from remote-sensing observations in the corona

In this section, we derive the magnetic, geometric, and kinematic CME parameters from remote-sensing observations, which we then use to initialise the CMEs in the heliospheric simulations. In this work, the CMEs are modelled as magnetic flux ropes (defined as bundles of twisted magnetic field lines with electric fields flowing inside; Antiochos et al. 1999; Török & Kliem 2005). First, the chirality and the orientation of the erupting flux rope are constrained from the CME source region proxies in Sect. 3.1. Second, the magnetic flux is derived using statistical relations based on the X-ray flare intensity in Sect. 3.2. Finally, a 3D geometrical reconstruction is performed using remote sensing coronagraph observations from LASCO and STEREO-B in the corona below 0.1 au in Sect. 3.3.
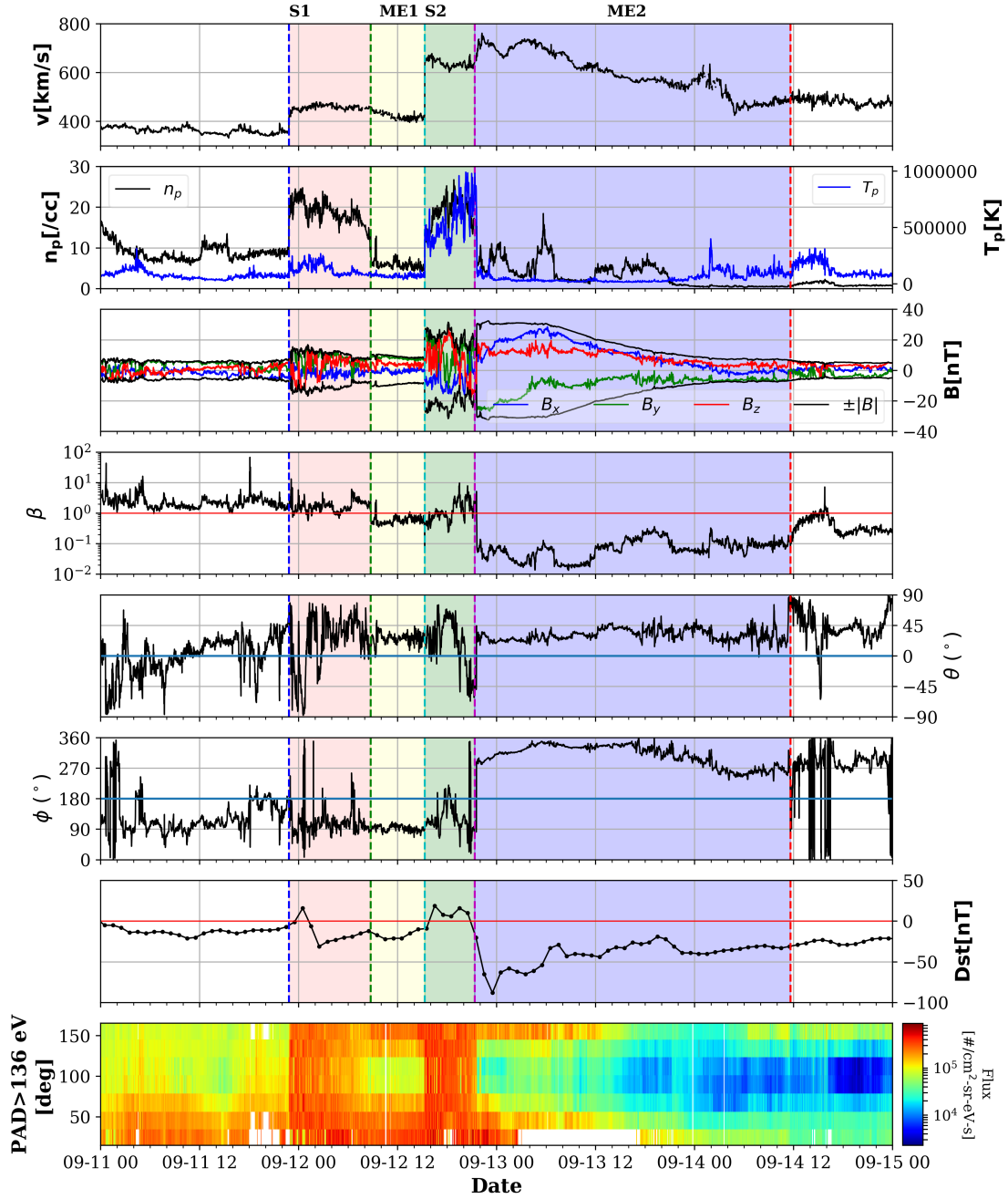
Fig. 4. In situ measurements by the Wind spacecraft during the period of September 11, 2014, and September 15, 2014. The figure shows (top to bottom) speed (v); proton temperature (T_p) and number density (n_p) in the second panel; magnetic field components (B_x, B_y, B_z) in the GSE coordinate system capped with the total magnetic field ($\pm|B|$) in the third panel; plasma beta (β) in the fourth panel; the θ and ϕ components of the magnetic field in GSE angular coordinates in the fifth and sixth panels, respectively; the Dst index in the seventh panel; and the suprathermal pitch angle distribution (with energies >136 eV) in the bottom panel. Vertical dashed lines indicate the shock arrival of CME1 (S1, blue) and the start of the magnetic ejecta passage of CME1 (ME1, green). The shock arrival of CME2 (S2, cyan), the start of the magnetic ejecta passage of CME2 (magenta), and the end of the magnetic ejecta passage (red) are as identified in the Wind ICME catalogue. The shaded red and yellow regions represent the sheath ahead of CME1 and the magnetic ejecta, ME1, respectively. The shaded green and blue regions depict the sheath ahead of the CME2 and the magnetic ejecta, ME2. The magnetic ejecta of CME2 has been identified in the Richardson and Cane catalogue as well.

3.1. Source region observations

In this section, we present our analysis of the magnetic field signatures during eruption of the CMEs –as well as those pre- and post-eruption– derived from remote sensing observations from the Atmospheric Imaging Assembly (AIA) and Helioseismic and Magnetic Imager (HMI) on board the Solar Disk Observatory (SDO; Lemen et al. 2012). AR 12158 appeared rotated

on the disc around September 3, 2014, and erupted twice, once on September 8 and again on September 10. Observations of the active region in different wavelengths during the eruption of CME1 and CME2 are shown in Figs. 5 and 6. We mainly focus on CME2 in order to understand its orientation during eruption and to probe the reasons for possible rotations in the low corona that could have led to the mismatch of its orientation at 1 au. To estimate the magnetic field orientation of the front part of
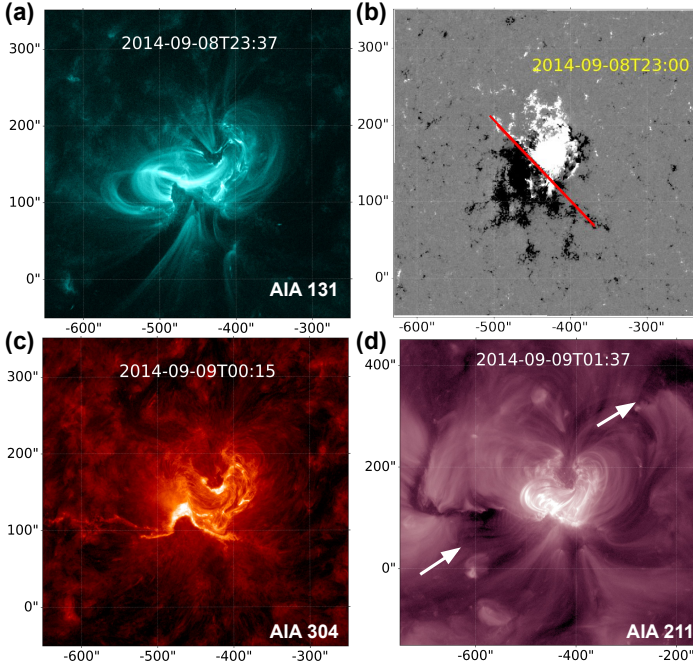
Fig. 5. AR 12158 associated with CME1 eruption in different wavelengths. (a) AIA 131 Å image highlighting the evolved sigmoid and the hooks corresponding to flux rope footpoints during the early phase of the flare. (b) HMI magnetogram saturated at ±200 G overlaid with the approximated PIL orientation (i.e. the part of the extended PIL that most likely erupted as CME1), before the start of the flare. (c) AIA 304 Å image showing the inverse J-shaped flare ribbons after the eruption, which suggest the eruption of a left-handed flux rope. (d) AIA 211 Å image showing the post-flare coronal dimmings (marked with white arrows). The *X*- and *Y*-axes correspond to the helio-projective longitude and latitude, respectively.

the flux rope, we investigate the magnetic chirality and polarity of the active region and the orientation of the polarity inversion line (PIL). In addition, we check the associated dimming regions to identify the footpoints of the erupting flux rope in order to further support the orientation inferred from the PIL.

Flux rope chirality (the sign of magnetic helicity). Using the EUV/soft-X-ray sigmoid as a proxy for an emerging flux rope embedded in an arcade (Titov & Démoulin 1999), a reverse S-shaped sigmoid is identified in AIA 131 Å before the eruption of CME1 and CME2 as shown in Figs. 5a and 6a, respectively. This suggests the erupting flux ropes associated with both CME1 and CME2 likely have a left-handed chirality. The leading positive magnetic polarity extends over the southern part of the trailing polarity and gives the active region a negative twist, which is a proxy for left-handed chirality (Luoni et al. 2011), as shown in the HMI magnetogram images in Figs. 5b and 6b. Additionally, the sigmoids were well identified with two inverse J-shaped flare ribbons in AIA 304 Å characterising their left-handedness in Figs. 5c and 6c for CME1 and CME2, respectively (Palmerio et al. 2017).

Flux-rope orientation. The orientation (tilt) of the erupting flux rope is inferred from the orientation of the PIL, which is usually parallel to the axial magnetic field of the flux rope. The tilt angle, measured from the solar west is assigned a positive (negative) value if the acute angle is calculated counterclockwise (clockwise) from the ecliptic on the solar west. The directionality of the axis is determined from the chirality of the active

region. The flare associated with CME1 was localised to the eastern part of the extended PIL, which could be approximated with a straight line, as shown in Fig. 5b. However, determining a univocal orientation for the PIL in the case of CME2 is not straightforward because the eruption extended along the curved geometry of the PIL (green dashed line in Fig. 6b). In the case of both CME1 and CME2, we consider the main axial field direction as northeastward, making an angle of ~−45° with the ecliptic. The magnetic field topology of AR 12158 reconstructed with a non-linear force-free field (NLFFF) model also corroborates the presence of a highly twisted pre-eruptive flux rope surrounded by inverse J-shaped magnetic field lines (Zhao et al. 2016). Dudík et al. (2016) found evidence of the occurrence of slipping reconnection in the flaring region where flare loops slip towards both ends of the ribbons. When the eruption occurs, the filaments are seen to be disturbed in AIA 171 Å in a northwestward direction, which was also identified by Dudík et al. (2016), as indicated by the white arrow in Fig. 6d. The locations of the footpoints of the flux rope are also identified with the coronal dimming signatures in AIA 211 Å, as shown in the white arrows in Fig. 6e. In Fig. 6f, the base difference image in AIA 131 Å is overlaid with the HMI magnetogram (saturated at ±1000 G; blue for positive and red for negative polarity) after the CME2 eruption. The development of the dark dimmings was observed in the southeast and northwest parts of the active region lying in the negative and positive magnetic polarity regions as marked by yellow circles. This suggests that the flux rope erupted almost parallel to the linear PIL marked by the red dashed line. The orientation of the main PIL of AR 12158 associated with the CME1 and CME2 eruptions is consistent with the descriptions provided by Vemareddy et al. (2016a), Dudík et al. (2016), Zhao et al. (2016), that is, the tilt is ~−45° using a straight-line assumption.

The conclusions drawn from the observations of the flare–CME eruption phase are as follows: (a) the axial flux rope fields of the CMEs are directed eastward; and (b) the CMEs were characterised by a left-handed helicity, which, combined with the eastward axial fields, implies north-to-south poloidal field lines at the flux rope apex, characterising the magnetic topology of the flux ropes as south-east-north (Bothmer & Schwenn 1998).

3.2. Deriving the reconnected magnetic flux associated with the CMEs (near 1 R⊙)

The amount of reconnected magnetic flux is derived using flare–CME statistical relations derived in previous works, as adopted in Scolini et al. (2020). The relations between the flare peak intensity in soft X-rays and the reconnected flux derived from the flare ribbons and coronal dimmings (Kazachenko et al. 2017; Dissauer et al. 2018; Tschernitz et al. 2018) are applied. Once the reconnected flux is obtained, the toroidal flux is derived based on the magnetic topology of the CME model. The statistical relations between the reconnected flux ϕ_r (in units of Mx) and the flare peak intensity, I_{SXR} (in units of W m^{-2}) used in this study are as follows:

(1) Kazachenko et al. (2017): Flare ribbon proxy:

$$\log_{10}(\phi_r) = 24.42 + 0.64\log_{10}(I_{\mathrm{SXR}}). \tag{1}$$

(2) Dissauer et al. (2018): Coronal dimming proxy:

$$\log_{10}(\phi_r) = 23.26 + 0.42\log_{10}(I_{\mathrm{SXR}}). \tag{2}$$

(3) Tschernitz et al. (2018): Flare ribbon proxy:

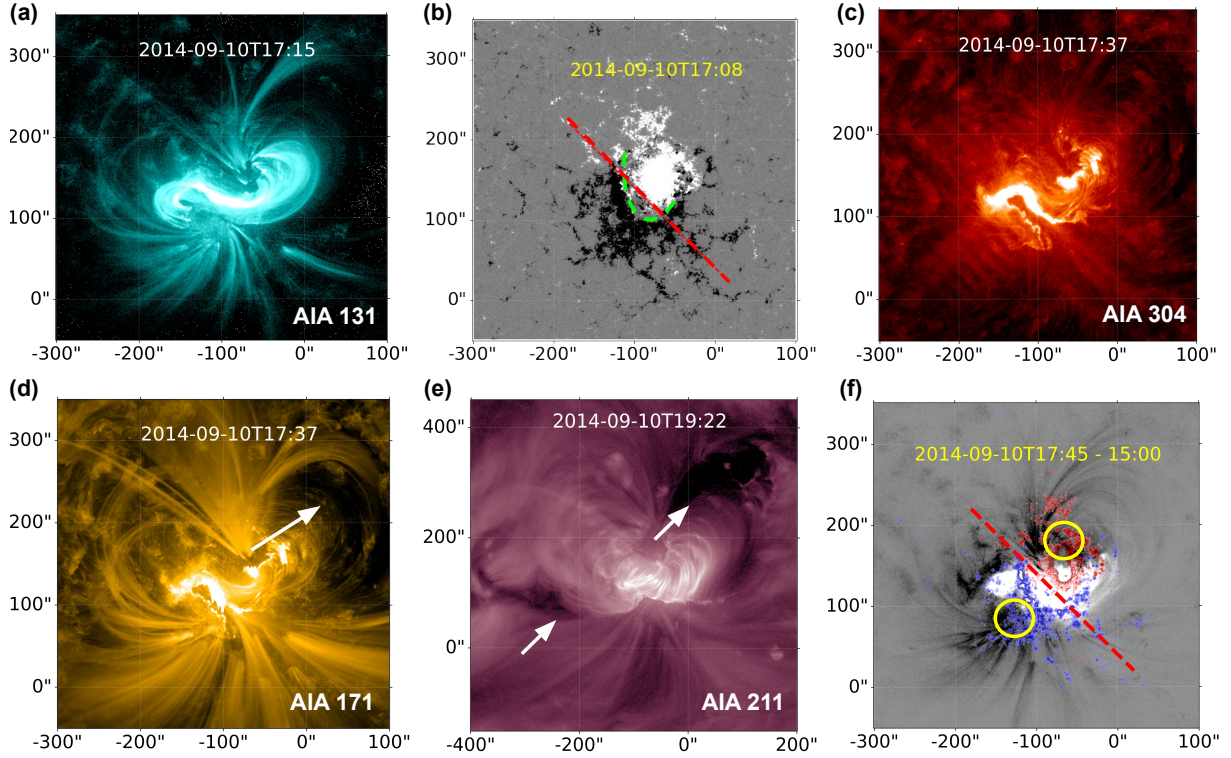$$\log_{10}(\phi_r) = 24.21 + 0.58\log_{10}(I_{\mathrm{SXR}}). \tag{3}$$

Fig. 6. AR 12158 associated with CME2 eruption in different wavelengths. (a) AIA 131 Å image before CME2 eruption. (b) HMI magnetogram saturated at ±200 G overlaid with the approximated PIL drawn with a red dashed line. (c) AIA 304 Å image highlights the inverse J-shaped flare ribbons indicating left-handedness of the flux rope. (d) AIA 171 Å image showing the coronal loops and the eruption direction of CME2 in north-westward direction as per Dudík et al. (2016). (e) AIA 211 Å image showing coronal dimmings marked with white arrows. (f) AIA 131 Å base-difference image overlaid with HMI magnetogram contours saturated at ±1000 G coloured blue and red for negative and positive polarity, respectively. The yellow circles demarcate the dimmings located at the footpoints of the FR. The red dashed line is the approximated PIL. The X- and Y-axes correspond to the helio-projective longitude and latitude, respectively.

The values of ϕ_r computed from the above relations and their averages are reported for CME1 ($I_{SXR} = 4.5 \times 10^{-5} \, \mathrm{W \, m^{-2}}$) and CME2 ($I_{SXR} = 1.6 \times 10^{-4} \, \mathrm{W \, m^{-2}}$) in Table 2. We follow the method for the conversion of ϕ_r to toroidal flux (ϕ_t) for the linear force-free spheromak model (hereafter referred to as the sphero- mak model; Chandrasekhar & Woltjer 1958; Shiota & Kataoka 2016) from Scolini et al. (2019), which yields a value (rounded off to the closest integer) of $\phi_t = 5 \times 10^{13} \, \mathrm{Wb}$ for CME1. For the Flux Rope in 3D (FRi3D; Isavnin 2016) model, we follow the FRED method of Gopalswamy et al. (2018) modified for the FRi3D geometry (refer to Appendix A), which results in a total flux (rounded off to the closest integer) of $\phi_{tot} = \phi_t + \phi_p = 1 \times 10^{14} \, \mathrm{Wb}$ for CME2. We note that the magnetic flux of the CME2 can also be derived by fitting the FRi3D model to the in situ observations (as in Sect. 4.1), and the reason we prefer to use this estimate is described in Sect. 5.3. The choice of employ- ing the spheromak and the FRi3D models for CME1 and CME2, respectively, is explained in Sect. 5.

3.3. CME kinematics and geometry in the corona

On September 9, 2014, Earth was at a longitudinal separation of 167° and 161° from STEREO-A and STEREO-B respec- tively (see Fig. 2). Due to a data gap in STEREO-A dur- ing this period, white-light coronagraph images from only two viewpoints, that is STEREO-B and LASCO, were used in the reconstruction. STEREO-A did not record data during this time. Although the observations by STEREO-B provided an

additional vantage point for the reconstruction, its location on the back side of the Sun made the projected view of the CMEs close to halo CMEs, which made the 3D reconstruction more challenging. The 3D reconstruction of CME1 was performed using the Graduated Cylindrical Shell (GCS; Thernisien 2011) model to constrain the geometrical parameters for the spheromak model, which are used in the EUHFORIA simulations in Sect. 5. The GCS parameters (in Stonyhurst coordinates) for CME1 are listed in Table 3: CME latitude (θ), longitude (ϕ), face-on (α) and edge-on (δ) angular half-widths, aspect ratio ($\kappa = \sin\delta$), and tilt (γ). The deprojected (3D) speed of the CME leading edge is v_{3D}, which is the sum of the radial speed (v_{rad}, speed of the CME centre) and the expansion speed (v_{exp}, rate of increase in the CME cross-section). The leading edge of the CME is tracked temporally to derive the v_{3D}. The spheromak model is launched with $v_{rad} = v_{3D}/(1 + \kappa)$ so that the CME cross-section expands self-consistently in the MHD heliospheric domain due to the Lorentz force (Scolini et al. 2019). The CME radius of the spheromak model at $21.5 \, R_\odot$ is given by $21.5 \sin(\alpha+\delta) \, R_\odot$. The reconstructed images are shown in Fig. B.1 in LASCO C3 (top) and STEREO-B (bottom) FOVs. As CME2 is simulated with the FRi3D model (further information in Sect. 5), its 3D reconstruction is performed with the FRi3D forward-modelling tool in order to appropriately constrain the parameters for the simulation. The parameters obtained from the fitting are listed in Table 3: CME latitude (θ), longitude (ϕ), angular half-width (φ_{hw}) and half-height (φ_{hh}), toroidal height (R_t), tilt (γ), flatten- ing (n), and pancaking (φ_p). Toroidal speed (v_{R_t}) and poloidal

Table 2. Reconnected flux using statistical relation based on flare intensity observations.

Reconnected flux from statistical relations ($\times 10^{21}$Mx)	CME1	CME2
Kazachenko et al. (2017) (ribbons)	4.41	9.79
Dissauer et al. (2018) (coronal dimmings)	2.74	4.63
Tschernitz et al. (2018) (ribbons)	4.94	10.2
Average	4.03	8.21

Table 3. Parameters from the GCS fitting of CME1 and the FRi3D fitting of CME2.

GCS parameters	CME1	FRi3D parameters	CME2
θ	17°	θ	24°
ϕ	−29°	ϕ	15°
α	46°	φ_{hw}	50°
κ	0.4	φ_{hh}	30°
γ	−55°	γ	45°
v_{3D}	696 km s^{-1}	$v_{R_{\mathrm{t}}}$	580 km s^{-1}
v_{rad}	497 km s^{-1}	$v_{R_{\mathrm{p}}}$	363 km s^{-1}
r_{spr}	21 $R_{\odot}$		
		n	0.5
		φ_{p}	0.5

speed ($v_{R_{\mathrm{p}}}$) are computed from the temporal fitting of the CME evolution and are similar to v_{rad} and v_{exp}, respectively, as mentioned in the context of the spheromak model. The FRi3D model fitted to CME2 in COR-2B and C3 FOV are plotted in Fig. B.2. Using the total speed constrained from the 3D reconstruction and assuming self-similar expansion in the upper corona, we compute the time of injection of the CMEs at the 0.1 au EUHFORIA boundary.

The position of CME2 obtained from the 3D reconstruction is consistent with the northwestward deflection of the CME and suggests a close-to-flank encounter at Earth if self-similarly extrapolated up to 1 au. Although two viewpoints are reported to improve the reconstruction (Verbeke et al. 2022), CME1 and CME2 were observed as halo by both LASCO and STEREO-B, which could increase the error in the especially critical parameters, such as speed and half-angle (Kay et al. 2020). Although the tilt (geometrical inclination) of the fitted flux rope is obtained from this methodology of geometrical reconstruction, the axial magnetic field is ambiguous, that is, it can be either east-to-west or west-to-east. As it is not straightforward to estimate the vector magnetic field in the middle-to-high corona, we rely on the in situ observations to determine the magnetic field components and hence the flux rope orientation. In the following section, in situ observations are used to constrain the CME2 magnetic field orientation at 1 au.

4. Reconstruction of CME2 from in situ observations at 1 au

The in situ magnetic field observations of ME2 from the Earth-bound WIND spacecraft are fit with the FRi3D, Linear Force-Free (LFF), and Circular-Cylindrical (CC) models to derive the chirality and the magnetic axis orientation of the flux rope at 1 au. Multiple models are used for validation purposes. The three selected models have cylindrical or modified-cylindrical configurations and involve the effect of the self-similar expansion of the flux rope, which makes the fittings more realistic (as shown

by Vemareddy et al. 2016b). In addition to constraining and verifying the magnetic field parameters, the motivation behind the in situ fitting is to investigate any rotation between 0.1 au and 1 au. As CME1 has no clear rotations in the magnetic field components at 1 au, we perform the fittings only for CME2. The comparison of the CME2 orientation near $1\,R_{\odot}$, at the corona, and at 1 au is presented at the end of this section.

4.1. FRi3D model

The numerical iterative fitting of the FRi3D flux rope to the in situ observations of ME2 is performed using a real-valued version of the genetic algorithm, as introduced in Isavnin (2016). The magnetic field in the FRi3D model is defined by the Lundquist model (Lundquist 1950). The flux-rope expansion is implemented by constructing a linearly growing CME cross-section into the model. In this model, the tilt parameter provides the latitudinal inclination (positive for counterclockwise and negative for clockwise from the ecliptic on the solar west), and the polarity determines the azimuthal direction (westward is +1; eastward is −1) of the magnetic field axis. The chirality is negative (positive) for right-handed (left-handed), which is opposite to the standard convention. A detailed description of the parameters can be found in Maharana et al. (2022). The FRi3D fitting (in green), as shown in Fig. 7(a), yields a westward left-handed flux rope with a tilt of +55°. This fitting also provides an estimate of the total magnetic flux of 0.5×10^{14} Wb and a twist of ~1.5 associated with CME2 at 1 au.

4.2. Linear Force Free model

Two fits were obtained by employing the LFF model, which incorporates the Lundquist magnetic field configuration (Lundquist 1950) with two different chiralities (H): positive ($H = +1$) and negative ($H = −1$). The results shown in Fig. 7a (in red for $H = +1$ and in blue for $H = −1$) consistently agree on the following: (i) the flux rope axis direction ($\theta \sim 25°$,
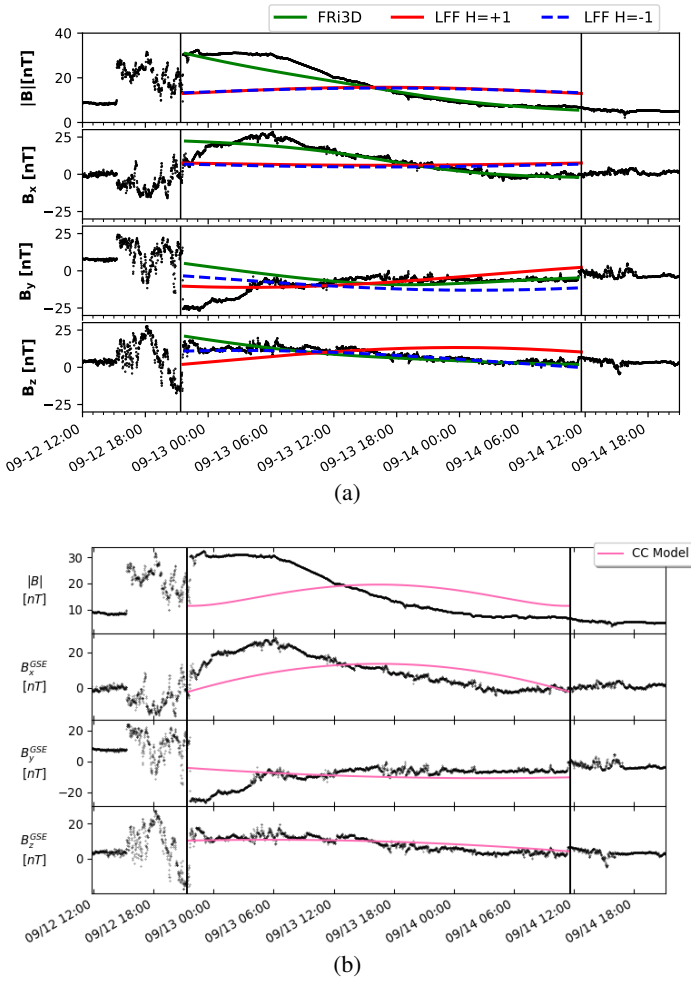
Fig. 7. Fitting of in situ observations of ME2 at 1 au with various models: (a) FRi3D model (green), LFF fit with right-handed chirality (red), and LFF fit with left-handed chirality (blue); (b) CC fit adapted from the WIND ICME catalogue (Nieves-Chinchilla et al. 2018). The vertical lines in black in both plots correspond to the ME2 boundary as per the same catalogue. The fitted parameters of the model are discussed in Sects. 4.1–4.3.

$\phi \sim -150°$); (ii) the high impact angle ($|z_0| \sim 0.88$), implying the passage of Earth far away from the axis of the ideal cylindrical structure assumed by the model, and (iii) the low chi-square of both these fits, which reflects high uncertainty in the fitting. As flux-rope chirality remains unchanged during heliospheric propagation (Palmerio et al. 2018), we consider the LFF fitting results with negative chirality based on the source region signatures.

4.3. Circular-cylindrical model

The analysis of the in situ signatures with the circular-cylindrical analytical flux rope model (CC model; Nieves-Chinchilla et al. 2016) is adapted from the WIND ICME catalogue[8] (Nieves-Chinchilla et al. 2018) (see Fig. 7d). The magnetic field configuration of this model is based on the non-force-free approach by relating the magnetic field vector with its current density, as proposed by Hidalgo et al. (2002b). In this model,

---

the cross-section distortion, expansion, curvature, and deformation are implemented following Hidalgo et al. (2002a) to reconcile CME with ICME from in situ, remote sensing, and MHD simulation perspectives. The orientation of the flux rope quantified by the latitude, $\theta = 9°$ (positive) and the longitude, $\phi = 350°$ (>180°), corresponds to a low-inclined northwestward flux rope. Negative helicity suggests the left-handedness of the ME. The impact parameter, $|y_0| \sim 0.9R$, implies that the smallest distance of the spacecraft to the flux rope axis (y_0) relative to the flux rope radius (R) is almost at the edge of the flux rope boundary.

The conclusions from the different in situ reconstruction techniques are: (a) the axial magnetic field of ME2 has a northwest orientation at 1 au, (b) the flux rope is left-handed, and (c) there is a high impact parameter, which implies a flank encounter. It must be noted that the uncertainty associated with determining the exact flux-rope orientation increases in cases with high impact parameters as compared to the head-on impacts (Riley et al. 2004; Al-Haddad et al. 2013). The conclusions (a) and (b) suggest that the magnetic topology of CME2 is northwest-south (NWS) (Bothmer & Schwenn 1998) at 1 au, contrary to south-east-north (SEN) as inferred close to $1 R_\odot$ in Sect. 3.1.

4.4. Discrepancy in CME2 orientation from observations at different locations

The analysis of the flux rope during the eruption in Sect. 3.1 suggests an SEN topology. However, an analysis of the in situ signatures of the magnetic ejecta at 1 au points to an NWS topology. This discrepancy in the flux-rope orientation retrieved for CME2 at the Sun and at 1 au is the focus of our investigation in the following sections. As per the PIL orientation of the CME2 source (Fig. 6b), the flux-rope orientation can be approximated to SEN pointing in the northeast direction. However, the details of the eruption from Dudík et al. (2016) and Vemareddy et al. (2016a) suggest a shearing rotation and deflection motion that could have led to the eruption of a southeast pointing SEN flux rope. The two possible cases are depicted in Fig. 8a. Cho et al. (2017) also estimate the PIL orientation of the CME2 to be southeast SEN during the eruption. The claim of rotation is also supported by the substantially quick (faster than typical Alfven speed) slipping and southward displacement of the eastern footpoint of the sigmoidal feature during the impulsive phase of the flare (Gou et al. 2023). Close to 0.1 au, CME2 can have two axial magnetic field directions for the same geometrical tilt as shown in Fig. 8b: either SEN or NWS. We therefore propose two possible scenarios: First, assuming a dominant low coronal rotation and no significant rotation in the inner heliosphere (0.1 au to 1 au), the northwestward-directed tilt constrained close to 0.1 au (hereafter, $\text{tilt}_{0.1\,\text{au}}^{\text{NWS}}$) is consistent with the tilt constrained at 1 au (hereafter, $\text{tilt}_{1\,\text{au}}$ as in Fig. 8c). The repercussion of this assumption is a physical rotation of CME2 by $\sim 180°-270°$ (assuming uncertainties in defining the PIL) in an anticlockwise direction owing to the left-handed chirality of the CME (Green et al. 2007; Lynch et al. 2009). Vemareddy et al. (2016a) suggest the eruption of CME2 was triggered by a helical kink instability driven by sunspot rotation. Such kink-unstable magnetic flux ropes are known to produce CME rotation in the low corona by converting their twist into writhe (Kliem et al. 2012), which could have resulted in such a significant rotation of CME2. The second scenario suggests a partial anticlockwise rotation in the low corona, leading to the southeast SEN flux rope at 0.1 au ($\text{tilt}_{0.1\,\text{au}}^{\text{SEN}}$), followed by an additional rotation in the heliosphere by about $\sim 180-270°$ to reach the reconstructed $\text{tilt}_{1\,\text{au}}$ at 1 au. The
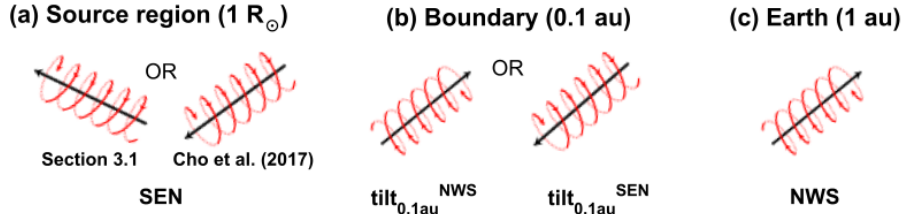
Fig. 8. Schematic representation of the CME2 orientation inferred from different observational proxies at different locations. (a) Close to 1 $R_\odot$, based on the analysis of the source region in Sect. 3.1 and the analysis of Cho et al. (2017); (b) close to 0.1 au, based on the 3D reconstruction of the white-light images (Sect. 3.3); and (c) at 1 au, based on the in situ observations (Sect. 4).

second scenario seems less probable, as previous studies suggest that most CMEs cease to undergo significant rotation and deflection at larger heliospheric distances and instead propagate self-similarly further away from the Sun (Démoulin & Dasso 2009; Isavnin et al. 2014; Balmaceda et al. 2020). We investigate the possibility of these two scenarios with numerical simulations in the following section.

5. MHD modelling with EUHFORIA

In this section, we present the simulation setup of the heliospheric propagation of the CMEs using the physics-based MHD model EUropean Heliospheric FORecasting Information Asset (EUHFORIA Pomoell & Poedts 2018). The aim here is to match the observations at 1 au measured by the WIND spacecraft. We specifically want to (1) find the orientation of CME2 at 0.1 au that needs to be injected to obtain the correct signature of ME2, and (b) understand the role of CME1 in forming the magnetic field rotation in the sheath region of CME2.

5.1. EUHFORIA setup

EUHFORIA consists of two parts: a coronal domain and a heliospheric domain. The coronal part is a 3D semi-empirical model based on the Wang-Sheeley-Arge (WSA, Arge et al. 2004) model, which provides the solar wind plasma conditions at the inner boundary of EUHFORIA, that is, 0.1 au. The WSA model is driven by the photospheric magnetic field via synoptic magnetogram maps. More details about the coronal model can be found in Pomoell & Poedts (2018) and Asvestari et al. (2019). The heliospheric part is a 3D time-dependent model of the inner heliosphere that numerically solves the ideal MHD equations –including gravity– using a cell-average finite volume method in the Heliocentric Earth EQuatorial (HEEQ) coordinate system. The constrained transport approach is applied to advance the magnetic field components in a divergence-free way. The boundary conditions at 0.1 au of this part are obtained from the coronal model. The computational domain extends from 0.1 au to 2 au in the radial direction, ±80° in the latitudinal direction, and 0–360° in the longitudinal direction. EUHFORIA enables the injection of the CMEs at the inner boundary as time-dependent boundary conditions, which are then self-consistently evolved by MHD equations. There are three functional CME models: (1) the cone model (Pomoell & Poedts 2018), which is a simplified non-magnetised spherical blob of plasma; (2) the LFF spheromak model (Verbeke et al. 2019), an improvement over the cone model by the inclusion of an internal magnetic field configuration; and (3) the FRi3D model (Maharana et al. 2022), which is an upgrade over the spherical shape of the spheromak model for improving the modelling of flank encounters and deformations. We used EUHFORIA version 2.0 for the simu-
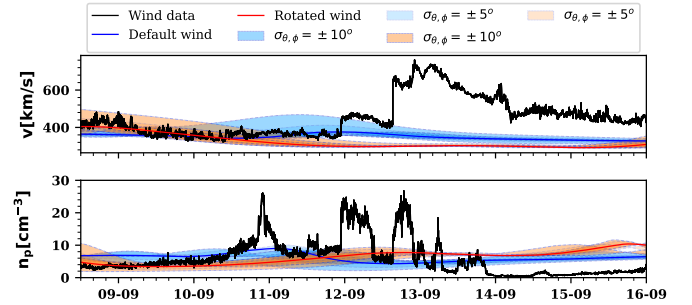

Fig. 9. Background solar wind modelled with the default EUHFORIA coronal model setup using the synoptic magnetogram from GONG on September 8, 2014, at 23:00 (in blue), and the rotated solar wind (in red). The shaded regions provide an error estimate in ±5–10° in latitude (σ_θ) and longitude (σ_ϕ) around Earth. Corresponding WIND observations are plotted in black.

lations in this work. The radial resolution of the computational mesh is 0.0074 au (corresponding to 1.596 $R_\odot$) for 256 cells in the radial direction, and the angular resolution is 4° in the latitudinal and 2° in the longitudinal directions, respectively.

5.2. The background solar wind

We perform the first EUHFORIA simulation by evolving the solar wind as a boundary condition without the insertion of CMEs to obtain an optimal ambient medium with reasonable plasma properties in which CMEs can propagate. The background solar wind is modelled using the synoptic magnetogram from the Global Oscillation Network Group (GONG) on September 8, 2014, at 23:00 UT (mrbqs140908t2314c2154_055.fits.gz). With this magnetogram fed as the boundary condition to the default coronal model of EUHFORIA, we obtained a high-speed stream traversing through Earth with its peak reaching ~3 days later as compared to the in situ observations. Hence, we rotated the inner boundary map of extrapolated solar wind plasma and magnetic field properties by 40° westward in order to make the high-speed stream arrive earlier at Earth and to more accurately reproduce the actual CME propagation and its position with respect to the high-speed stream. The speed and the proton number density profiles from both simulations, the default wind (in blue) and the rotated wind (in red), are shown in Fig. 9.

5.3. Modelling the CMEs

In this work, we employ the spheromak model and the FRi3D model to simulate CME1 and CME2, respectively. We refrain from modelling both CMEs with FRi3D due to an

implementation limitation affecting the injection of consecutive FRi3D CMEs into the heliospheric domain. As the legs of a first CME simulated with FRi3D would remain connected to the inner boundary, the insertion of a second CME would raise numerical complications. As the main focus of this study is CME2, FRi3D is used for improved modelling of the magnetic field components and the spheromak model is used for CME1. We first experimented with using the spheromak model to simulate both CMEs. When CME2 was modelled with spheromak, the CME had to be launched almost along the Sun–Earth line (although the real CME2 event was a flank encounter) in order to model its interaction with CME1. This is because of the inability of the spheromak model to reproduce the flank impact of CME2 due to the lack of CME legs in the model. Recent studies point to additional drawbacks of using the spheromak model to model the interplanetary propagation of CMEs. The magnetic moment of the spheromak model tends to tilt and align itself with the magnetic field of the ambient solar wind. As the spheromak model is not anchored to the Sun, as is the case of real CME, it is free to undergo unrealistic rotation in the heliosphere due to the spheromak tilting instability (Asvestari et al. 2022). Therefore, this model cannot be used to investigate the possible rotation of the CMEs in interplanetary space. We had to adjust the density of the spheromak model in an ad hoc manner to limit the inherent spheromak tilting. This resulted in an overestimated number density profile of CME2, and yet the magnetic field profiles of CME2 were not appropriately reproduced. Due to the numerical constraint of using the FRi3D model to simulate both the CMEs consecutively, we chose to use the spheromak model for CME1 and shifted it towards the Sun–Earth line in a calculated manner to represent the leg of CME1. We constrain the CME input parameters for the spheromak and the FRi3D model following the methods described by Verbeke et al. (2019), Scolini et al. (2019), and Maharana et al. (2022). The geometrical and kinematic parameters are obtained from the 3D reconstruction of the CMEs in the solar corona as detailed in Sect. 3.3. The magnetic field parameters for the CME models are constrained using observations of the source region as detailed in Sect. 3.2. All the parameters are summarised in Table 4.

We perform three numerical experiments (Run1, Run2, and Run3), each involving one CME (CME1 or CME2), in order to determine the parameters of the individual CMEs at the heliospheric boundary that match the observations at 1 au. The results of these experiments are used to perform the final simulation (Run4) involving both the CMEs. With the first two simulations, labelled Run1 and Run2, we aim to investigate the orientation of CME2 that must be injected at 0.1 au in order to reproduce the magnetic field components when propagated to 1 au, before introducing CME1 ahead of it. All the parameters corresponding to the FRi3D model are kept the same in these two runs, except for the polarity. Run1 is initialised with a southeastward $\text{tilt}_{0.1\,\text{au}}^{\text{SEN}}$ and Run2 with a northwestward directed $\text{tilt}_{0.1\,\text{au}}^{\text{NWS}}$. The magnetic flux value used for the FRi3D model in Run1 and Run2 is 0.5×10^{14} Wb, which is half the value constrained near the photospheric surface ($1\,R_\odot$) in Sect. 3. This value is not ad hoc, but is consistent with the total magnetic flux value constrained from the fitting of the FRi3D model to the in situ observations at 1 au in Sect. 4.1. Maharana et al. (2022) showed that the FRi3D model expands faster and arrives earlier when initialised with the magnetic flux value constrained using the methodology involving the remote-sensing observations, and can therefore be initialised with a lower flux estimated from in situ observations for better prediction accuracy. In Run3, only CME1 is simulated with the spheromak model in order to assess its independent signature at Earth. The fourth simulation, Run4, is

Table 4. CME parameters used in the EUHFORIA simulations employing the spheromak model for CME1 in Run3 and Run4, and the FRi3D model for CME2 in Run1, Run2, and Run4.

Input parameters		
	CME1	CME2
CME model	Spheromak	FRi3D
Geometrical		
Insertion time	2014-09-09 04:24 UT	2014-09-10 20:14 UT
Speed	450 km s^{-1}	500 km s^{-1}
Latitude	22°	24°
Longitude	−14°	15°
Half-width	–	50°
Half-height	–	30°
Radius	21 $R_\odot$	–
Toroidal height	–	13.6 $R_\odot$
Magnetic field		
Chirality	−1	+1 [(*)]
Polarity	–	+1(−1)
Tilt	−135° [(**)]	45°
Toroidal magnetic flux	5×10^{13} Wb	–
Total magnetic flux	–	5×10^{13} Wb
Twist	–	1.5
Deformation		
Flattening	–	0.5
Pancaking	–	0.5
Plasma parameters		
Mass density	10^{-18} kg m^{-3}	10^{-17} kg m^{-3}
Temperature	0.8×10^6 K	0.8×10^6 K

Notes. The only change for Run1 is in the polarity parameter of the FRi3D model, which is −1 (eastward) as opposed to +1 (westward) for Run2 and Run4. [(*)]FRi3D chirality is implemented with an opposite convention, −1 for right-handedness and +1 for left-handedness. [(**)]Conventionally, a left-handed tilt of 0° configuration of the spheromak model is a westward flux-rope normal to the Sun–Earth line. Therefore, with the eastward tilt of 45°, the spheromak model is rotated anticlockwise by 135°, i.e. −135°.

designed to allow us to investigate the effect of CME1 in preconditioning the propagation of CME2, and the influence of CME–CME interaction on the geoeffectiveness of the impact at Earth. Run4 uses the input parameters of CME1 from Run3, and those of CME2 from the best simulation between Run1 and Run2 based on the results of Sect. 6.1. In Run3 and Run4, the mass density used for the spheromak model is 10^{-18} kg m^{-3}, which is an order of magnitude lower than the mass density used for the FRi3D model (i.e. 10^{-17} kg m^{-3}). According to Maharana et al. (2022), the typical volume of the flux-rope geometry (as in the case of FRi3D) requires a higher standard density in the order of 10^{-17} kg m^{-3} (supported by observations in Temmer et al. 2021) to enhance the modelling accuracy of mass of a CME modelled with FRi3D at 0.1 au. However, the spherical volume of the spheromak model is up to 2–3 orders of magnitude higher than that of the FRi3D model and therefore a comparable mass can be modelled with a lower density of 10^{-18} kg m^{-3}. Therefore, CME1 and CME2 have different initial mass densities depending on the CME model used. As the geometrical reconstruction points to a glancing blow of CME1 at Earth and the spheromak model does not possess legs, it is possible to miss the effect of its flank encounter on the interaction with CME2. Hence, we shift CME1 ∼ 15° westward in longitude and ∼5° northward in

Table 5. EUHFORIA simulations, the CME models used, and the time of arrival of the shocks (ToA; datetime in yyyy-mm-dd HH:MM format) of the CMEs at Earth in the EUHFORIA simulations.

Simulations	CME1	CME2
Run1	–	FRi3D $\left(\text{tilt}_{0.1\,\text{au}}^{\text{SEN}}\right)$ (2014-09-12 18:13 UT)
Run2	–	FRi3D $\left(\text{tilt}_{0.1\,\text{au}}^{\text{NWS}}\right)$ (2014-09-12 18:23 UT)
Run3	Spheromak (2014-09-11 23:23 UT)	–
Run4	Spheromak (2014-09-11 23:23 UT)	FRi3D $\left(\text{tilt}_{\text{au}}^{\text{NWS}}\right)$ (2014-09-12 12:33 UT)
Observed ToA	2014-09-11 22:50 UT	2014-09-12 15:17 UT

Notes. The observed ToA of the CMEs from the Wind ICME catalogue is provided for comparison.

latitude in order to better reproduce the effect of its legs in Run4. In the simulation domain, we place virtual spacecraft around Earth separated by an angular distance of 5° and 10° in latitude and longitude, respectively, in order to capture the variability of the results in the vicinity of Earth. Additional virtual spacecraft are placed along the Sun–Earth line with a radial separation of 0.1 au to track the radial evolution of the CMEs.

6. Simulation results and discussion

A summary of the EUHFORIA simulations performed in this study, including the CME models used for each CME and the time of arrival of the corresponding CME shock (ToA, datetime in yyyy-mm-dd HH:MM format) of the CMEs in the simulations, is provided in Table 5.

6.1. Propagation of CME2 only

A comparison of Run1 and Run2 is shown in Fig. 10. Speed and density are modelled similarly in both cases. The arrival time of CME2 in both Run1 and Run2 is delayed by ~3 h as compared to the observed ToA of the shock. Using $\text{tilt}_{0.1\,\text{au}}^{\text{NWS}}$ in Run2, the prolonged positive B_z component is well reproduced and the negative B_y component better matches observations compared to the use of $\text{tilt}_{0.1\,\text{au}}^{\text{SEN}}$ in Run1. Through this experiment, we developed an understanding of the circumstances that led to the formation of the positive B_z component in ME2 instead of the predicted prolonged negative B_z component. Run1 ($\text{tilt}_{0.1\,\text{au}}^{\text{SEN}}$) does not seem to rotate significantly in the heliospheric domain of our simulation to match the observations at 1 au ($\text{tilt}_{0.1\,\text{au}}^{\text{NWS}}$). This suggests that the flux rope must have undergone rotation in the corona (i.e. within 0.1 au) up to reaching $\text{tilt}_{0.1\,\text{au}}^{\text{NWS}}$, where it would then have propagated in the heliosphere without significant rotation resulting in the observed magnetic field profile at 1 au.

6.2. Propagation of CME1 only

In this section, we discuss the results of Run3. We first initialised the CME with v_{rad} = 497 km s^{-1}, and yet the CME arrived
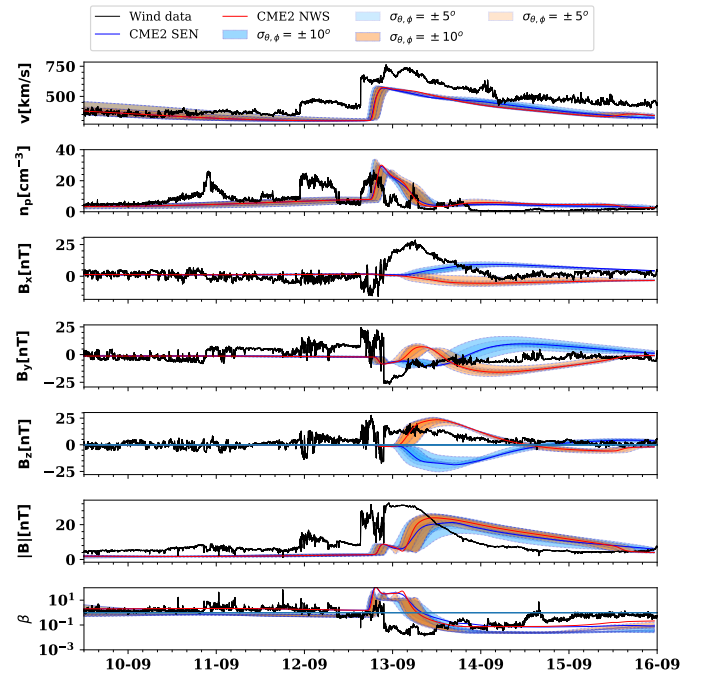
Fig. 10. Time series plot showing a comparison between the simulations with different orientations of CME2 modelled with FRi3D, at Earth: Run1 (blue) is simulated with $\text{tilt}_{0.1\,\text{au}}^{\text{SEN}}$ (deduced based on the orientation close to 1 $R_\odot$) and Run2 (red) with $\text{tilt}_{0.1\,\text{au}}^{\text{NWS}}$ (similar to the tilt at 1 au). Both the orientations follow the same geometrical tilt derived from the 3D reconstruction at 0.1 au but with two different axial magnetic field orientations. From top to bottom: Speed (v), proton number density (n_p), B_x, B_y, B_z, magnetic field strength ($|B|$), and plasma beta (β). The solid line and the shaded regions show the profile at Earth and in the 5–10° latitudinal and longitudinal offset around Earth, respectively.

at Earth ~4 h earlier than the observed time of arrival. As the main purpose of this study is to understand the CME magnetic field signatures rather than to predict the CME arrival times, we optimised the v_{rad} to 450 km s^{-1} in order to model the latter interaction with CME2 in Run4 more accurately. The modelled time series of the physical parameters at Earth are presented in Fig. 11. After reducing the CME speed as described above, the shock of CME1 is modelled to arrive on 2014-09-11 at 23:23 UT (43 min later than the actual CME1 arrival), as visible in the sharp increases in the speed and proton density profiles. The drop in β on ~2014-09-12 at 12:00 UT is due to the passage of ME1 at its flank, that is, the southwest portion of the magnetic ejecta associated with CME1 (see figures in Sect. 6.3). There is no clear rotation in the magnetic field components. A leading positive B_z signature is obtained (slightly overestimated) followed by a weak trailing negative B_z component.

6.3. Propagation of CME1 followed by CME2

Based on the previous runs, we find that the most accurate modelling of the CME2 signatures at 1 au (in Run4) arises from the simulation of CME1 as in Run3 and of CME2 as in Run2. The results of Run4 are discussed and compared to Run2 in this section. In Fig. 12, the plasma and magnetic field properties of Run4 are over-plotted on the results of Run2 so that we can distinguish the features due to the possible CME–CME interaction in the presence of CME1 in Run4. The solid vertical lines in blue, green, cyan, and magenta correspond to S1, the start of ME1, S2, and the start of ME2 in Run4. The shaded regions
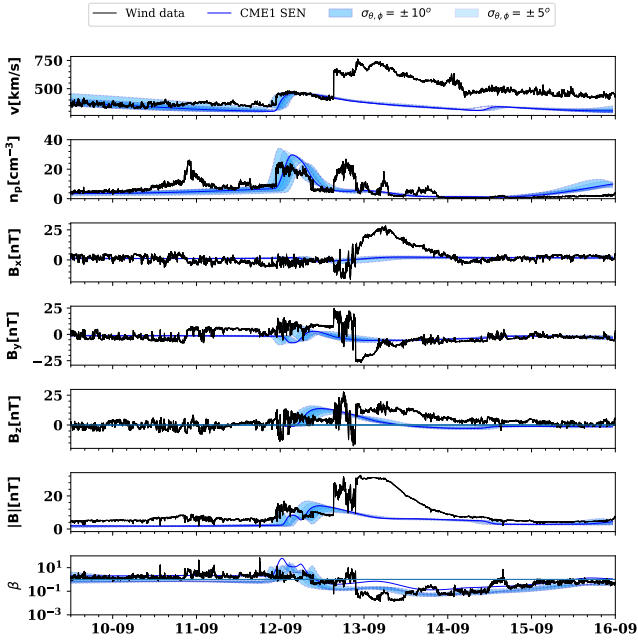
Fig. 11. Results of Run3 where CME1 is modelled with the spheromak model. The figure description is similar to that of Fig. 10.

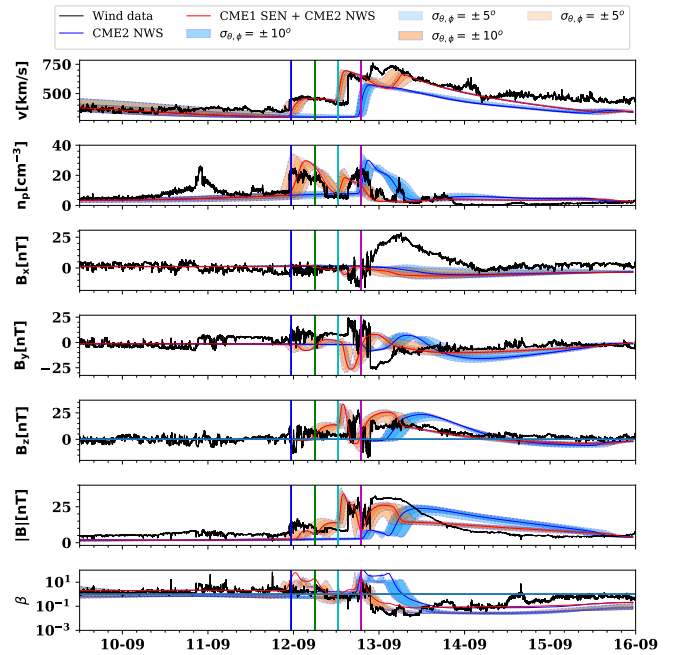**Fig. 12.** Results of Run2 (blue; CME2 NWS) and Run4 (red; CME1 SEN + CME2 NWS) are compared. CME1 and CME2 parameters in Run4 correspond to Run3 and Run2, respectively. Figure description is similar to Fig. 10. S1, the start of ME1, S2, and the start of ME2 are marked with blue, green, cyan, and magenta vertical lines, respectively, in Run4.

around the solid line of the simulation time series represent the same physical properties in the vicinity of ±5–10° in latitude (σ_θ) and longitude (σ_ϕ) around Earth. We first analyse the speed and number density in the time series plot at Earth to compare the effect of CME1 in Run4. In the absence of CME1 (Run2), CME2 arrived at Earth ~3 h later than observations, while in the presence of CME1 (Run4), CME2 arrived at Earth ~3 h earlier with respect to the observations, implying that it was sped up by ~6 h by CME1. The passage of CME1 creates a low-density region ahead of CME2 that allows it to expand faster, leading to a higher shock speed and a depletion in density inside the flux rope (the n_p peak is lower in Run4 than Run2). In Run4, the difference between the arrival time of the CMEs is ~13 h. It is to be noted that ToA is the arrival time of the CME shock. The sheath and the magnetic ejecta following the shocks are extended structures in the radial direction (the magnetic ejecta alone can be up to 0.5 au in radial size at 1 au for very large or expanding events). Therefore, even if the CME2 shock arrives 16 h after the CME1 shock, this does not imply the absence of interaction between the two structures. The trailing part of ME1 is in fact interacting with CME2 in this case.

Second, we analyse the magnetic field signatures of CME2 in Run4 and highlight the additional features due to the presence of CME1. The first weak drop in β_p (proton plasma beta, i.e., $\beta/2$) at ~2014-09-12 06:00 UT is modelled in Run4, while it was missing in Run2, which reaffirms the short passage of ME1. The drop in β_p at ~2014-09-12 19:00 UT in Run4 corresponds to the starting of ME2 and matches the observations well. The period when $\beta_p < 1$ continues beyond the actual observed end time of ME2 due to the over-expansion of the CMEs in the simulation. The B_x component is not significantly affected, but additional structures are observed in the B_y and B_z components in the sheath region ahead of CME2 in Run4 as compared to Run2. A strong drop in the B_y component up to −27 nT in the sheath at 2014-09-12 16:00 UT, although overestimated, qualitatively corresponds to B_y = −13 nT at ~2014-09-12 18:20 UT in the in situ observations. This is followed by a short-lasting increase to

positive B_y = 9 nT at ~ 2014-09-12 22:50 UT and a long-lasting negative B_y corresponding to ME2. The following feature, that is, the transition of the positive B_y to long-lasting negative B_y, is sharp in observations. The sheath and the magnetic ejecta of CME2 are reasonably well reproduced in Run4. The sheath has an enhanced positive B_z = 33 nT at ~2014-09-12 14:00 UT (28 nT at 2014-09-12 18:08 UT in situ) followed by a negative B_z = −5 nT (−17 nT at 2014-09-12 20:57 UT in situ), which is clearly missing in Run2. Both simulations similarly capture the prolonged positive B_z in ME2. The strength of the minimum negative B_z component in the sheath is underestimated at Earth. The virtual spacecraft at $\sigma_{\theta,\phi}$ = ±10° from Earth registered a minimum B_z = −11 nT around 2014-09-12 19:00 UT, which is closer to the in situ observations. Due to the overestimation of B_y in the sheath, the total magnetic field in the sheath is also overestimated.

We also provide the radial evolution plots for Run4 in Fig. 13 in order to understand the evolution of the magnetic ejecta (especially B_z) along the Sun–Earth line at different times during the propagation of both the CMEs. B_{clt} (the co-latitudinal component in the spherical coordinate system) is plotted in the equatorial and the meridional plane for Run4 in Fig. 14 for a 2D view of the process. B_{clt} is equivalent to $-B_z$ on the equatorial plane. The red and blue spectra of the colour bar correspond to positive and negative B_z, respectively. While referring to Fig. 14, we provide the description in terms of B_z instead of B_{clt} to discuss the phenomena. We discuss the results for two phases of the CME propagation process: pre-interaction and interaction.

Pre-interaction. Run4 gives similar results to Run3 in the pre-interaction phase until 2014-09-12 12:33 UT. In Fig. 14a, the leading part of the magnetic ejecta associated with CME1 can be observed to propagate with a positive B_z component
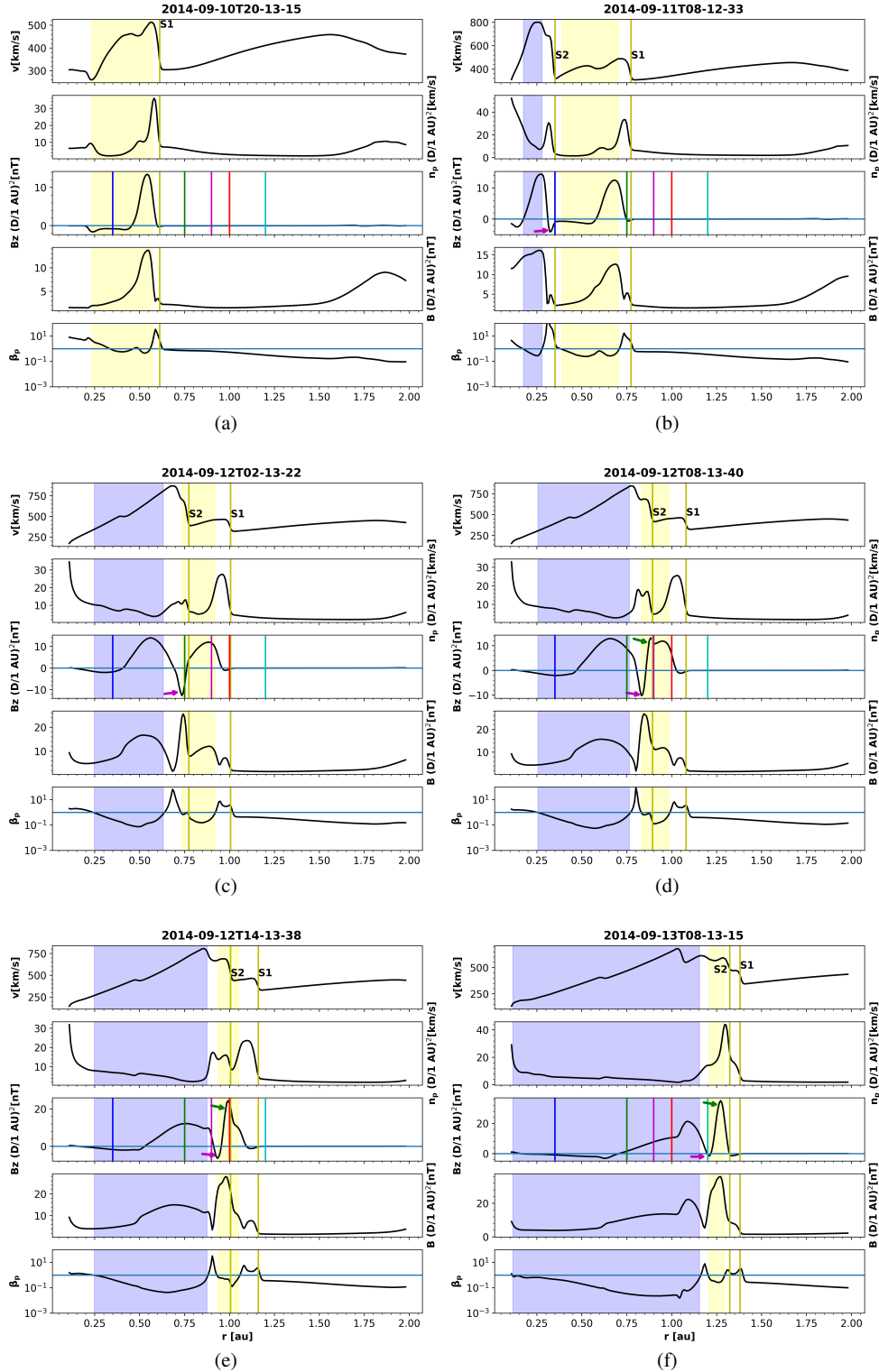
Fig. 13. Radial evolution profile of the CME1 and CME2 along the Sun–Earth line at different times of propagation and interaction extracted from Run4. Top to bottom (in each plot): speed (v), proton number density (n_p), z-component of magnetic field (B_z), total magnetic field (B), and proton plasma beta (β_p). The yellow and blue shaded areas depict the extent of magnetic ejecta of CME1 and CME2, respectively, extracted using the criterion $\beta_p < 1$ ($\beta_p < 5$ in (a)). All physical quantities except the speed are scaled by $(D/1\,\mathrm{au})^2$ where D is the radial distance from the Sun. The CME shocks (S1 and S2) are marked in yellow lines. The colourful vertical lines in the B_z panel correspond to different radial distances, which help to explain the various phases of Run4 (detailed in Sect. 6.3): (a) Propagation of CME1 alone in the heliosphere; (b) formation of a compressed negative B_z ejecta CE1a (shown with the magenta arrow); (c) further compression of CE1a; (d) development of a compressed positive B_z ejecta, CE1b (shown with a green arrow), ahead of CE1a; (e) further compression of CE1b; and (f) diffusion of CE1a ($\sim$0 nT) upon reaching 1.2 au while CE1b undergoes further enhancement.
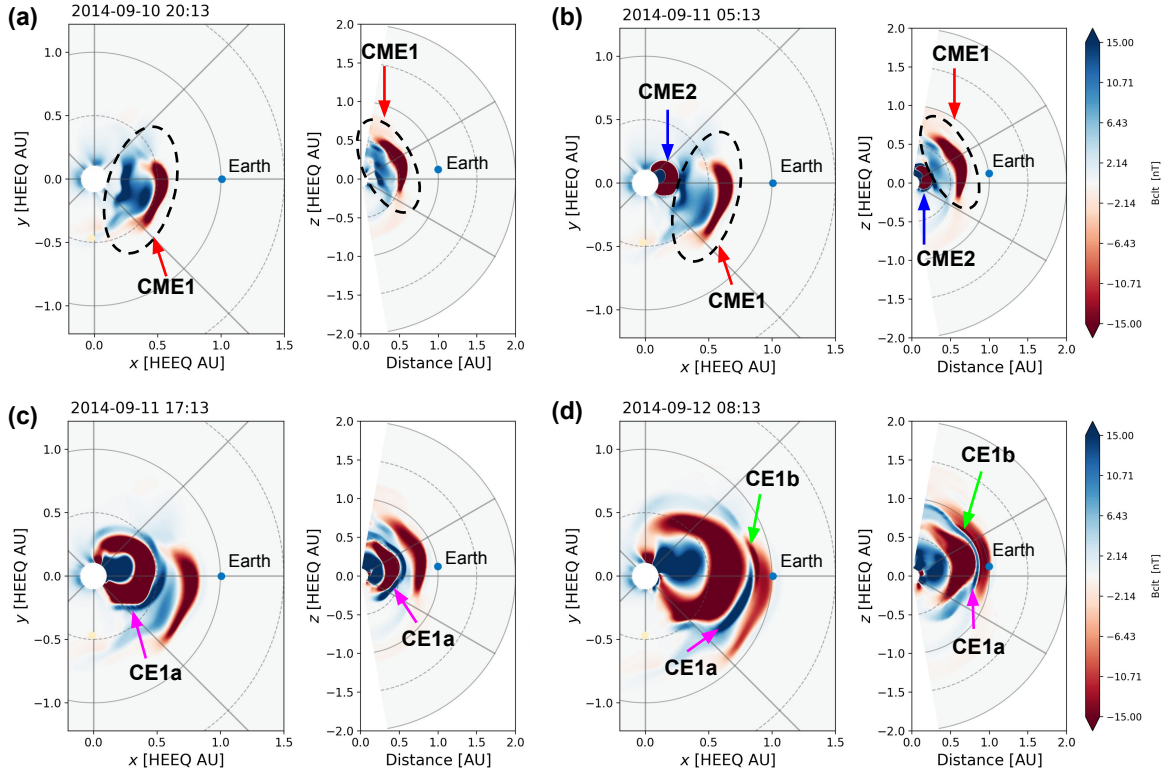
Fig. 14. Evolution of B_z in the heliosphere as simulated in Run4. The co-latitudinal component in the spherical coordinate system is B_{clt}, which is equivalent to $-B_z$ on the ecliptic plane. The red and blue spectra of the colour bar correspond to positive and negative B_z, respectively. Each of the panels (a) to (d) shows the view of the equatorial (X–Y) plane and the meridional (X–Z) plane at a particular time, mentioned at the top of each. (a) CME1 in the pre-interaction phase is identified schematically with a dashed ellipse; (b) CME2 is shown evolving behind CME1 in the early stage of interaction; (c) CME2 is seen compressing the interval of the trailing negative B_z component of CME1 to create CE1a (darker blue region) in the sheath ahead of itself; and (d) CE1a is seen to be further compressing the interval of the leading positive B_z component of CME1 to create CE1b (darker red region) during the interaction phase of the event. The animation of this figure can be found online.

followed by a negative B_z component, and the same signatures are reproduced in situ when ME1 arrives at Earth (Fig. 12).

Interaction. In Fig. 13, the vertical yellow lines corresponding to the shock of the CMEs (S1 and S2) and the other coloured vertical lines in the B_z panel marking different locations (radial distances) from the Sun are used for the purpose of description in this section. The yellow and blue shaded areas mark the extent of magnetic ejecta of CME1 and CME2, respectively, extracted using the criterion $\beta_p < 1$ in all figures except for Fig. 13a. The criterion of low n_p, in combination with $\beta_p < 5$, is used to identify the CME1 extent below 0.5 au in Fig. 13a. This shows the phase where CME1 has propagated alone in the heliosphere with a dominant positive B_z component (>10 nT), followed by a weak minimum negative B_z component (~−2 nT), and has reached 0.65 au at 2014-09-10 20:13 UT. The extent of CME1 in the equatorial and meridional planes of the heliospheric domain can be observed in Fig. 14a. In the next phase in Fig. 13b, CME2 has entered the heliospheric domain and its shock has reached 0.35 au (marked by yellow lines). An enhancement of the negative B_z component interval of the ejecta (hereafter, compressed ejecta 1, CE1a) to ~−4 nT is observed in the CME2 sheath at 2014-09-11 08:13 UT just before 0.35 au (vertical blue line). This enhancement is present in the sheath region as the corresponding $\beta_p > 1$ and can be interpreted as the interval of trailing negative B_z component of CME1 being compressed by CME2. CME1 appears weaker than CME2 as it is the flank of

the CME1 that hits Earth and the magnetic field strength of a flux rope becomes weaker away from its axis. In our simulations, we observe that CME1 expands rapidly in the heliosphere and therefore has a larger trailing part extending up to ~0.2 au, while the leading part has reached ~0.6 au (Fig. 14b). This explains how CME2 (faster than CME1) was able catch up with CME1 and start compressing it below 0.5 au. Figure 14c shows the prominent development of CE1a at 2014-09-11 17:13 UT. Figure 13c shows CE1a (marked with a magenta arrow in the B_z panel) in the CME2 sheath being further compressed to $B_z < -10$ nT as it reaches 0.75 au at 2014-09-12 02:13 UT, while the CME1 shock reaches ~1 au (vertical red line). A strong positive $B_z > 10$ nT in the region of $\beta < 1$ up to 0.7 au corresponds to ME2, which seems to be pushing CE1a further. The next phase depicted in Fig. 13d is the development of an enhancement in the interval of the leading positive B_z component of CME1 ahead of CE1a (hereafter, compressed ejecta 2, CE1b, marked with a green arrow in B_z panel) at 0.9 au (vertical magenta line) at 2014-09-12 08:13 UT. From Figs. 14c and d, CE1a can be seen to compress the interval of the leading positive B_z component of ME1 to create CE1b. It must be noted that these features are very thin and localised. Figure 13e shows the further enhancement of CE1b at 1 au with a $B_z > 20$ nT, which is more than the maximum $B_z \sim 10$ nT inside ME1. CE1a begins to weaken and is of lower magnitude at 2014-09-12 14:13 UT as compared to the in situ observations. However, when CE1a was at 0.9 au, the minimum negative B_z better matched the 1 au observations. In addition, it is evident from Fig. 14d that the most enhanced

part of CE1a (i.e. minimum B_z component) is to the east of the Sun–Earth line and to the north of the ecliptic. The enhanced features are quite small compared to the prominent magnetic ejecta in the event and are sufficiently localised to be easily missed while reading out the 3D data at a single point in the simulation. Figure 13f shows the phase where CE1a has a very weak magnetic field strength upon reaching 1.2 au (vertical cyan line) at 2014-09-13 08:13 UT, while CE1b is further compressed. CE1a seems to have been compressed between ME2 and CE1b. The propagation of the CME2 shock (the trailing vertical yellow line) towards the CME1 shock (the leading vertical yellow line) can be observed through Figs. 13c–f. The CME2 shock moves across the $\beta < 1$ region associated with CME1, along the Sun–Earth line, which can be inferred as a signature of interaction. Moreover, the $\beta_p < 1$ part associated with CME1 gets narrower in time, which points to the subsequent increase in compression by CME2.

6.4. Parameters affecting the sheath formation

The width and the duration of the compressed features in the sheath of CME2 (the CME that propagates behind CME1 and compresses it while catching up with it) depend on the relative speed between the two CMEs and on the physical properties of both CMEs, such as their shape and size (Russell & Mulligan 2002). Additional simulations were performed (whose detailed results are not shown in this paper) to analyse the effect of these parameters on the formation of the features in the sheath ahead of CME2. The duration of a particular feature, for example, CE1b, depends on the compression induced by CE1a on the B_z profile (with intervals of negative and positive values) of CME1 during their propagation through the interplanetary space. If CME1 is slower (i.e. in the case of a lower relative speed), CME2 can catch up with it earlier and can compress the interval with the negative B_z component of CME1 more, generating a thinner and diffused CE1b by the time they arrive at 1 au. We also find in our simulations that, for a faster CME1 (i.e. in the case of a higher relative speed), CE1a catches up with the interval with the positive B_z component of CME1 to form CE1b at a later time. In this case, the compression takes place beyond the Earth's orbit, and the simulation fails to capture the enhanced positive B_z signature in the sheath before the negative B_z signature. Given the short spatio-temporal nature of these distinct features, these dynamics can be easily missed if virtual spacecraft are not taken into consideration. The minimum B_z strength of CE1a at 1 au is indeed captured by the spacecraft at 10° longitudinal offset from Earth rather than the solid red line at Earth in Run4 (Fig. 12). The magnetic field strength of the compressed ejecta depends on the flux contained in CME1. Moreover, if the magnetic field configuration of CME1 was not modelled correctly, then the B_y and B_z features in the sheath would have had different signs and may have resulted in completely different features in the sheath. The shape and size of CME1 also play an important role in the morphology of the compressed ejecta. The flux and twist of CME2 not only influence its magnetic field strength obtained at 1 au but also its ability to compress the ejecta ahead. This event clearly depicts how the sheath region carries the history of the minute interactions between different magnetic ejecta, which might be challenging to predict based on remote-sensing observations. Although 3D MHD simulations help in modelling and understanding such interactions better, it can still be challenging to precisely reproduce the observed features owing to the sensitivity of the simulations to the uncertainties in the initial parameters, as discussed above.

7. Summary and conclusions

In this study, we present the evolution of two successive CMEs that erupted from the active region AR 12158 on September 8, 2014, and September 10, 2014, respectively. The motivation of this work is to investigate the misinterpretation of certain observational aspects related to the CMEs and to reproduce their in situ signatures at 1 au using MHD simulations. The first CME was not predicted to hit Earth and was not even recorded in the ICME catalogues. The second CME was predicted to be geoeffective based on the remote observations of the CME chirality and magnetic axis orientation during the eruption. However, unexpectedly, upon arrival at Earth, its magnetic ejecta was dominated by a positive B_z component. Nonetheless, a short period of negative B_z component developed in the sheath of CME2 during its propagation in the heliosphere. This resulted in a geomagnetic storm with a Dst index of ∼−88 nT at Earth, which is a moderate value and not an extreme value as was originally predicted. Therefore predictions of the geoeffectiveness of the various substructures involved in this event were gravely inaccurate. The study of this event is based on the observational investigation of the CMEs, and the 3D MHD modelling of their evolution using EUHFORIA. We performed an in-depth analysis of the two CMEs using remote sensing and in situ observations, and constrained the geometrical and magnetic field parameters successively, close to $1\,R_\odot$, close to 0.1 au, and at 1 au. A discrepancy was observed in the axial magnetic field orientation of CME2 between $1\,R_\odot$ and 0.1 au. Our motivations for performing numerical experiments involving CME1 and CME2 individually (Run1, Run2, Run3) and the global EUHFORIA simulation including CME1 and CME2 (Run4) are as follows:

- Run1: We first performed a simulation including only CME2 using the FRi3D model in EUHFORIA, with the magnetic field orientation obtained close to $1\,R_\odot$. However, the results did not match the in situ magnetic field observations at 1 au.
- Run2: In order to determine the cause of this discrepancy, we performed another simulation with the initial magnetic field orientation consistent with in situ observations at 1 au using the FRi3D model in EUHFORIA. The inference of the new magnetic field orientation of CME2 is based on the 3D reconstruction (close to 0.1 au) and the assumption of anticlockwise rotation of left-handed CME2 in the low corona (based on the relationship between the chirality and the rotation direction from Green et al. 2007; Lynch et al. 2009). Run2 is able to reproduce the prolonged positive B_z component seen in the in situ observations and matches the observations much better than Run1. However, Run2 requires a significant ∼180°−270° rotation of CME2 in the low corona which remains to be explained, as no rotation is observed during the heliospheric propagation in the simulations.
- Run3: After obtaining the best simulation of CME2, we performed a simulation including just CME1 with the spheromak model. The magnetic field orientation of CME1 close to $1\,R_\odot$ was consistent with the orientation obtained close to 0.1 au and was used to obtain the best simulation of CME1 to reproduce the in situ signatures at 1 au.
- Run4: Finally, we introduced CME1 and CME2 using the boundary conditions found in Run3 and Run2 to create the final global simulation (Run4). The kinematics and the magnetic field components of the CMEs were successfully modelled at Earth with the magnetised flux rope CME models in EUHFORIA. The interaction between CME1 and CME2 was found to produce the short interval of negative B_z component in the sheath ahead of CME2. With the 3D MHD

EUHFORIA simulation, it was possible to understand the different phases of the CME1–CME2 interaction and how they form coherent enhanced substructures (CE1a and CE1b) in the sheath region.

In summary, we investigated the reasons for the erroneous predictions of space weather linked to this event. We find these to be two-fold: first, the consideration of a low coronal rotation of CME2 was missed, which led to the prediction of a different magnetic field topology heading towards Earth; second, the presence of CME1 was overlooked and therefore the geoeffective feature formed by its interaction with CME2 was not predicted. EUHFORIA in its present version allows us to propagate the CMEs in the heliosphere. We showed that a substantial rotation of CME does not take place in the heliosphere. Therefore, we suggest that the rotation of CME2 could have occurred in the corona. With this study, we also highlight the importance of observations in correctly constraining simulations in order to obtain accurate space-weather forecasting.

Previous studies suggest that a significant amount of CME rotation, deflection, and deformation occurs in the low corona, followed by a self-similar propagation further away from the Sun in most CME events (Démoulin & Dasso 2009; Isavnin et al. 2014; Balmaceda et al. 2020). Kliem et al. (2012) , and more recently, Gou et al. (2023) highlighted the possibility of extensive low coronal rotation up to even more than $100°$ by the combination of twist and shear-driven rotation, the latter being dominant in the lower corona. It is not possible to verify the hypothesis of a substantial rotation ($\sim 180° - 270°$) of CME2 in the low corona under the scope of this work, as EUHFORIA does not account for the modelling of the initial CME evolution below 0.1 au. In addition, the lack of magnetic field observations in the corona prevents observational verification of this hypothesis. The speculation of substantial CME2 rotation in the low corona, although a relatively strong assumption, could justify the consistency of the CME2 orientation observed in the upper corona and at 1 au. Therefore, knowledge of the CME magnetic field is crucial for deriving the correct orientation of the emerging flux rope in the low corona, and therefore for propagating it further in the heliospheric models for space weather forecasting purposes. Although the white-light coronagraph images help to reconstruct the CMEs in the middle and upper corona, they are not sufficient to derive the magnetic field configuration. This leaves us to rely on the source region proxies for guessing the magnetic field configuration for prediction purposes, being agnostic to the dominant low coronal dynamics. Although the closest approach of Parker Solar Probe is in the upper corona, its trajectory does not act as a constant in situ monitoring point in the corona. The other forecasting limitation arises from the evolution of CME structures during their propagation, and their interaction with the solar wind and other CMEs. The interaction of CMEs may lead to severe geoeffective events, as demonstrated by Shen et al. (2018), Scolini et al. (2020), and Koehn et al. (2022). The lack of multiple in situ crossings through CME2 makes it challenging to predict its global behaviour through reconstruction using data from just a single point. Furthermore, for CME crossings with a high impact factor, single-point reconstruction techniques introduce greater uncertainty in the estimation of the flux-rope orientation (Riley et al. 2004). The serendipitous alignment of spacecraft such as PSP, Solar Orbiter, and Bepi Colombo, although helpful in obtaining information about the early phase of the CME, is also not feasible for constant monitoring. Without knowledge of the global behaviour of the individual CMEs, it is even more challenging and non-trivial to predict the strength and configuration of the magnetic ejecta formed during CME–CME interaction. We therefore propose that a stronger observational infrastructure is required for the study of CME–CME interaction events from the perspective of space-weather forecasting in addition to MHD simulations.

References

Al-Haddad, N., Nieves-Chinchilla, T., Savani, N. P., et al. 2013, Sol. Phys., 284, 129

An, J., Magara, T., Hayashi, K., & Moon, Y.-J. 2019, Sol. Phys., 294, 143

Antiochos, S. K., DeVore, C. R., & Klimchuk, J. A. 1999, ApJ, 510, 485

Arge, C. N., Luhmann, J. G., Odstrcil, D., Schrijver, C. J., & Li, Y. 2004, J. Atmos. Sol. Terr. Phys., 66, 1295

Asvestari, E., Heinemann, S. G., Temmer, M., et al. 2019, J. Geophys. Res. (Space Phys.), 124, 8280

Asvestari, E., Rindlisbacher, T., Pomoell, J., & Kilpua, E. K. J. 2022, ApJ, 926, 87

Balmaceda, L. A., Vourlidas, A., Stenborg, G., & St. Cyr, O. C. 2020, Sol. Phys., 295, 107

Bothmer, V., & Schwenn, R. 1998, Ann. Geophys., 16, 1

Brueckner, G. E., Howard, R. A., Koomen, M. J., et al. 1995, Sol. Phys., 162, 357

Burlaga, L. F. 1988, J. Geophys. Res., 93, 7217

Cane, H. V., & Richardson, I. G. 2003, J. Geophys. Res. (Space Phys.), 108, 1156

Chandrasekhar, S., & Woltjer, L. 1958, Proc. Nat. Academy Sci., 44, 285

Cheng, X., Ding, M. D., & Fang, C. 2015, ApJ, 804, 82

Cho, K. S., Marubashi, K., Kim, R. S., et al. 2017, J. Korean Astron. Soc., 50, 29

Démoulin, P., & Dasso, S. 2009, A&A, 498, 551

Dissauer, K., Veronig, A. M., Temmer, M., Podladchikova, T., & Vanninathan, K. 2018, ApJ, 855, 137

Dudík, J., Polito, V., Janvier, M., et al. 2016, ApJ, 823, 41

Gieseler, J., Dresing, N., Palmroos, C., et al. 2022, Front. Astron. Space Sci., 9, 384

Gopalswamy, N., Akiyama, S., Yashiro, S., & Xie, H. 2018, in Space Weather ofthe Heliosphere: Processes and Forecasts, eds. C.. Foullon, & O. E. Malandraki, 335, 258

Gosling, J. T., McComas, D. J., Phillips, J. L., & Bame, S. J. 1991, J. Geophys. Res., 96, 7831

Gou, T., Liu, R., Veronig, A. M., et al. 2023, Nat. Astron., in press [arXiv:2305.03217]

Green, L. M., Kliem, B., Török, T., van Driel-Gesztelyi, L., & Attrill, G. D. R. 2007, Sol. Phys., 246, 365

Hidalgo, M. A., Nieves-Chinchilla, T., & Cid, C. 2002a, Geophys. Res. Lett., 29, 1637

Hidalgo, M. A., Cid, C., Vinas, A. F., & Sequeiros, J. 2002b, J. Geophys. Res. (Space Phys.), 107, 1002

Huttunen, K. E. J., Schwenn, R., Bothmer, V., & Koskinen, H. E. J. 2005, Ann. Geophys., 23, 625

Isavnin, A. 2016, ApJ, 833, 267

Isavnin, A., Vourlidas, A., & Kilpua, E. K. J. 2014, Sol. Phys., 289, 2141

Kaiser, M. L., Kucera, T. A., Davila, J. M., et al. 2008, Space Sci. Rev., 136, 5

Kay, C., Mays, M. L., & Verbeke, C. 2020, Space Weather, 18, e02382

Kazachenko, M. D., Lynch, B. J., Welsch, B. T., & Sun, X. 2017, ApJ, 845, 49

Kilpua, E. K. J., Lumme, E., Andreeova, K., Isavnin, A., & Koskinen, H. E. J. 2015, J. Geophys. Res. (Space Phys.), 120, 4112

Kilpua, E. K. J., Pomoell, J., Price, D., Sarkar, R., & Asvestari, E. 2021, Front. Astron. Space Sci., 8, 35
Kliem, B., Török, T., & Thompson, W. T. 2012, Sol. Phys., 281, 137
Koehn, G. J., Desai, R. T., Davies, E. E., et al. 2022, ApJ, 941, 139
Lemen, J. R., Title, A. M., Akin, D. J., et al. 2012, Sol. Phys., 275, 17
Lundquist, S. 1950, Ark. Fys., 2, 361
Luoni, M. L., Démoulin, P., Mandrini, C. H., & van Driel-Gesztelyi, L. 2011, Sol. Phys., 270, 45
Lynch, B. J., Antiochos, S. K., Li, Y., Luhmann, J. G., & DeVore, C. R. 2009, ApJ, 697, 1918
Maharana, A., Isavnin, A., Scolini, C., et al. 2022, Adv. Space Res., 70, 1641
Marubashi, K., Cho, K. S., & Ishibashi, H. 2017, Sol. Phys., 292, 189
Nieves-Chinchilla, T., Linton, M. G., Hidalgo, M. A., et al. 2016, ApJ, 823, 27
Nieves-Chinchilla, T., Vourlidas, A., Raymond, J. C., et al. 2018, Sol. Phys., 293, 25
Palmerio, E., Kilpua, E. K. J., James, A. W., et al. 2017, Sol. Phys., 292, 39
Palmerio, E., Kilpua, E. K. J., Möstl, C., et al. 2018, Space Weather, 16, 442
Pomoell, J., & Poedts, S. 2018, J. Space Weather Space Clim., 8, A35
Richardson, I. G., & Cane, H. V. 2010, Sol. Phys., 264, 189
Riley, P., & Ben-Nun, M. 2021, Space Weather, 19, e02775
Riley, P., Linker, J. A., Lionello, R., et al. 2004, J. Atmos. Sol. Terr. Phys., 66, 1321

Russell, C. T., & Mulligan, T. 2002, Planet. Space Sci., 50, 527
Scolini, C., Rodriguez, L., Mierla, M., Pomoell, J., & Poedts, S. 2019, A&A, 626, A122
Scolini, C., Chané, E., Temmer, M., et al. 2020, ApJS, 247, 21
Shen, C., Xu, M., Wang, Y., Chi, Y., & Luo, B. 2018, ApJ, 861, 28
Shiota, D., & Kataoka, R. 2016, Space Weather, 14, 56
Temmer, M., Holzknecht, L., Dumbović, M., et al. 2021, J. Geophys. Res. (Space Phys.), 126, e28380
Thernisien, A. 2011, ApJS, 194, 33
Titov, V. S., & Démoulin, P. 1999, A&A, 351, 707
Török, T., & Kliem, B. 2005, ApJ, 630, L97
Tschernitz, J., Veronig, A. M., Thalmann, J. K., Hinterreiter, J., & Pötzi, W. 2018, ApJ, 853, 41
Vemareddy, P., Cheng, X., & Ravindra, B. 2016a, ApJ, 829, 24
Vemareddy, P., Möstl, C., Amerstorfer, T., et al. 2016b, ApJ, 828, 12
Verbeke, C., Pomoell, J., & Poedts, S. 2019, A&A, 627, A111
Verbeke, C., Mays, M. L., Kay, C., et al. 2022, Adv. Space Res.
Webb, D., & Nitta, N. 2017, Sol. Phys., 292, 142
Winslow, R. M., Lugaz, N., Philpott, L. C., et al. 2015, J. Geophys. Res. (Space Phys.), 120, 6101
Zhao, J., Gilchrist, S. A., Aulanier, G., et al. 2016, ApJ, 823, 62
Zurbuchen, T. H., & Richardson, I. G. 2006, Space Sci. Rev., 123, 31

Appendix A: FRi3D model flux calculation

The toroidal flux (ϕ_t) as a function of the poloidal flux (ϕ_p) for a flux rope with Lundquist magnetic field configuration is given by (Gopalswamy et al. 2018):

$$\phi_t = \phi_p \frac{2\pi R_0}{L} J_1(x_{01}), \qquad (A.1)$$

where R_0 and $L=2.6\ R_{tip}$ are the radius and length of the flux rope, respectively. R_{tip} is the leading edge of the flux rope. J_1 is the first-order Bessel function and x_{01} is the first zero of zeroth-order Bessel function, J_0. We modify the above formula for FRi3D geometry by replacing R_0 with the poloidal height of FRi3D (R_p) and L with the FRi3D axis length given by:

$$L = \int_{-\phi_{hw}}^{\phi_{hw}} \left[r(\phi)^2 + (\frac{dr(\phi)}{d\phi})^2 \right]^{\frac{1}{2}} d\phi, \qquad (A.2)$$

where $r(\phi) = R_t cos^n(a\phi)$ is the cross-section at a given ϕ and $a = (\pi/2)/\phi_{hw}$. R_t is the toroidal height and ϕ_{hw} is the angular half-width. Further details of FRi3D geometry and the parameters used here can be found in Maharana et al. (2022).

Appendix B: 3D reconstruction of the CMEs

The geometrical and kinematic parameters of CME1 and CME2 are constrained from the 3D reconstruction using the GCS model (Thernisien 2011) and the FRi3D model (Isavnin 2016), respectively. As CME1 is modelled with the spheromak model in EUH-FORIA simulations, it is reconstructed with the GCS model (Fig. B.1) as done in Verbeke et al. (2019), Scolini et al. (2019). CME2 is reconstructed with the FRi3D model (Fig. B.2) and modelled with the same in EUHFORIA.
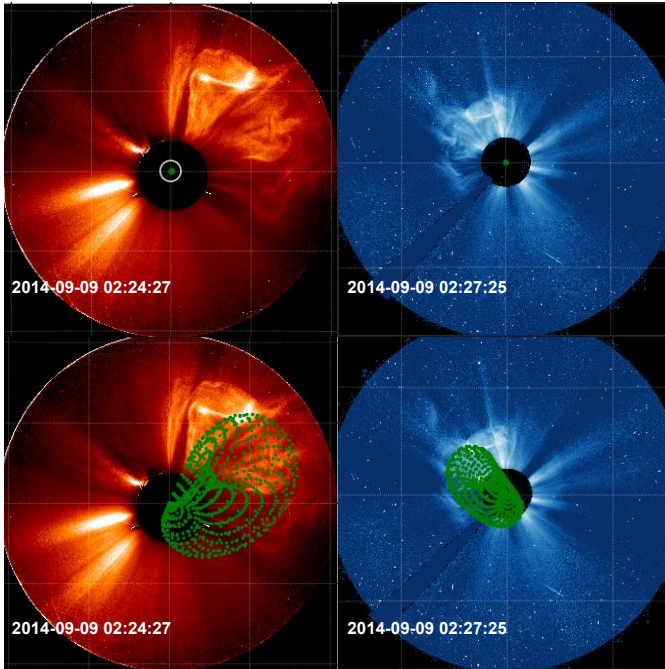

Fig. B.2. Coronagraph images of CME2 development on September 10, 2014, as observed by COR2 (STEREO-B) and C3 (LASCO) (top). The same images overlaid with the 3D reconstruction using the FRi3D model (bottom).

Fig. B.1. Coronagraph images of CME1 development on September 9, 2014, as observed by COR-2 (STEREO-B) and C3 (LASCO) (top). The same images overlaid with the 3D reconstructi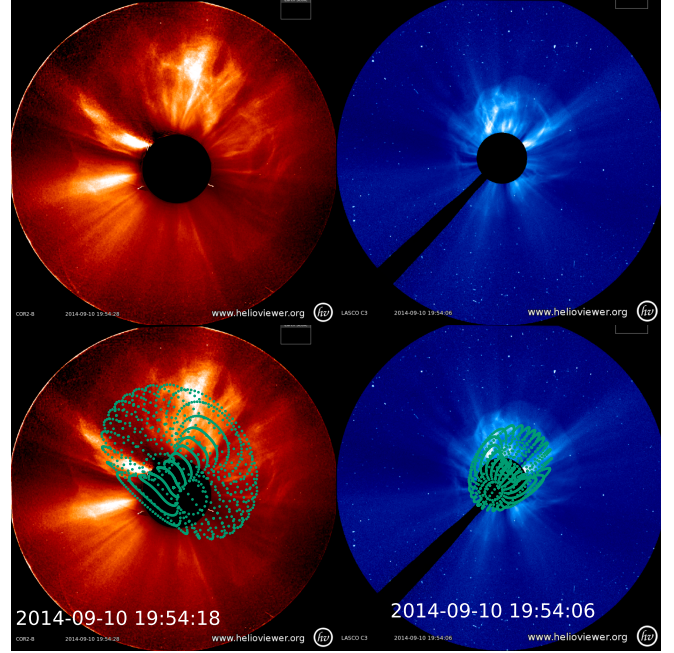on using the GCS model (bottom).